



Article

Mineralogy of Cobalt-Rich Ferromanganese Crusts from the Perth Abyssal Plain (E Indian Ocean)

Łukasz Maciąg ^{1,*}, Dominik Zawadzki ¹, Gabriela A. Kozub-Budzyń ², Adam Piestrzyński ², Ryszard A. Kotliński ¹ and Rafał J. Wróbel ³

¹ Faculty of Geosciences, Institute of Marine and Coastal Sciences, University of Szczecin, Mickiewicza 16A, 70383 Szczecin, Poland; dominik.zawadzki@usz.edu.pl (D.Z.); ryszard.kotlinski@usz.edu.pl (R.A.K.)

² Faculty of Geology, Geophysics and Environmental Protection, Department of Economic Geology, AGH University of Science and Technology, Mickiewicza 30, 30059 Kraków, Poland; lato@agh.edu.pl (G.A.K.-B.); piestrz@geol.agh.edu.pl (A.P.)

³ Faculty of Chemical Technology and Engineering, West Pomeranian University of Technology Szczecin, Pułaskiego 10, 70322 Szczecin, Poland; rafal.wrobel@zut.edu.pl

* Correspondence: lukasz.maciag@usz.edu.pl; Tel.: +48-91-444-2371

Received: 26 December 2018; Accepted: 27 January 2019; Published: 29 January 2019



Abstract: Mineralogy of phosphatized and zeolitized hydrogenous cobalt-rich ferromanganese crusts from Dirck Hartog Ridge (DHR), the Perth Abyssal Plain (PAP), formed on an altered basaltic substrate, is described. Detail studies of crusts were conducted using optical transmitted light microscopy, X-ray Powder Diffraction (XRD) and Energy Dispersive X-ray Fluorescence (EDXRF), Differential Thermal Analysis (DTA) and Electron Probe Microanalysis (EPMA). The major Fe-Mn mineral phases that form DHR crusts are low-crystalline vernadite, asbolane and a ferroxhyte-ferrihydrite mixture. Accessory minerals are Ca-hydroxyapatite, zeolites (Na-phillipsite, chabazite, heulandite-clinoptilolite), glauconite and several clay minerals (Fe-smectite, nontronite, celadonite) are identified in the basalt-crust border zone. The highest Ni, Cu and Co contents are observed in asbolane and Mn-(Fe) vernadite. There is significant enrichment of Ti in ferroxhyte-ferrihydrite and vernadite. The highest rare earth element (REE) content is measured in the phosphate minerals, less in phyllosilicates and Na-phillipsite. The geochemical composition of minerals in the DHR crusts supports the formation of crusts by initial alteration, phosphatization and zeolitization of the substrate basalts followed by oscillatory Fe-Mn oxyhydroxides precipitation of hydrogenous vernadite (oxic conditions) and diagenous asbolane (suboxic conditions).

Keywords: Fe-Mn oxyhydroxides; marine deposits; cobalt-rich ferromanganese crusts; hydrogenous crusts; Dirck Hartog Ridge; Perth Abyssal Plain; Indian Ocean

1. Introduction

Co-rich ferromanganese crusts formation and mineral composition have been the subject of several scientific works [1–8]. Recent discoveries from previously unstudied locations, mainly due to increase of marine research, provide new data on crusts chemistry, mineralogy, formation conditions and economic importance [9–12].

Cobalt-rich ferromanganese crusts consist of layered Fe-Mn oxyhydroxide deposits found on rock substrates at depths between 400 and 7000 m below sea level (mbsl), where ocean bottom currents clear rocks of sediment cover [13]. Maximum crusts thickness is around 26 cm; however, the mean thickness is only 3 cm. Crusts occur at the flanks and summits of conical seamounts, guyots, ridges, plateaus and other volcano-tectonic forms [14].

According to the cobalt-rich ferromanganese crusts classification based on types of fluids and seawater sources of elements (cold ambient bottom waters or medium to low temperature

hydrothermal fluids), the two major types of ferromanganese crusts are distinguished: (I) hydrogenetic cobalt-rich ferromanganese crusts; (II) hydrothermal crusts and encrustations (sometimes called stratabound manganese oxides) [15–18]. Hydrothermal crusts that precipitate directly from low temperature hydrothermal fluids (few tens of degrees up to 200 °C), usually grow significantly faster, even up to 1600–1800 mm/Ma [19]. Ferromanganese crusts in some locations form through a combination of fluid sources and thereby exhibit a mixed origin, primarily either hydrogenetic, diagenetic or hydrothermal-hydrogenetic [15,18,20,21].

Co-rich ferromanganese crusts formation is dominated by hydrogenetic processes. The precipitation from bottom waters is extremely slow, with growth rates of 1–5 mm/Ma. The thickest crusts occur in the depth interval between 800–2500 m and show the highest concentrations of critical metals [22]. Some authors limit this depth to the anoxic zone at approximate depths of 1000–1500 m. Below these depths, the thickness of crusts decrease [23–25].

On the youngest rock outcrops, crusts form mainly patina-thin layers. Most crust surfaces are either botryoidal, smooth or rough, that form under conditions of strong bottom currents. In the thick crusts, 2 to 8 visible or macroscopic layers may be distinguished. The internal layers are usually black and massive, while outer parts are slightly lighter, laminated and more porous [13]. However, crusts with four major layers of oxide layers have been found. The outer- and innermost are massive and show light colors, whereas the middle layer is porous and brown [5]. Some authors [26] divide phosphatized ($P_2O_5 > 0.7\%$) basal or relic “layer R” of Upper Cretaceous to upper Paleocene age and “layer I” as the oldest (subdivided into I-1 and I-2; Eocene) “anthracite” layer, which rests immediately on the substrate and show a very compact, massive texture and steel gray color. “Layer II” is an intermediate “dendritic” layer, brown in color, loose, and porous, with characteristic globular–dendritic structure, non-phosphatized and mostly of Miocene age. “Layer III” is the top youngest layer, contacting with water, which shows a thin-bedded texture and a dark brown color, usually of Pliocene to Quaternary age.

Under natural conditions, the crust formation is presumably a reversible process—rate of their growth could be sharply retarded or even replaced by dissolution depending redox conditions. This possibility is also supported by geological observations: clumpy porous surfaces of growing crusts occur together with lustrous smoothed areas, show signs of dissolution. The discordance between different age crusts layers, suggests few gaps in the formation. Metal concentrations in oceanic waters, compared to the crusts, are generally very low and cations can be incorporated in accordance with percolating–adsorptive properties of manganese minerals, if only bottom waters are constantly nourished with new portions of solution contact with the crusts surface. Delivery of metal ions from oceanic waters depends on the bottom currents velocity and spatial-temporal character of circulation [23,27].

The distinctive feature of ferromanganese crusts is high concentration of cobalt, ranging from 0.07 to 1.9% in bulk samples, with an average of 0.14–0.97% [28] and 0.19–0.74% [29] depending on source distance and oceanic region. Crusts, compared to polymetallic nodules (another marine ferromanganese deposit), contain less copper and nickel [14], however, they are highly enriched in lead, tellurium, cerium, europium and other elements, relative to seawater and continental crust [16]. Dominant factors determining the concentration of elements in hydrogenetic crusts include: concentration of each element in seawater, element-particle reactivity, oxidation degree of MnO_2 , elements residence time in seawater and growth rate [29].

The major aim of this paper is to present mineralogical description of cobalt-rich ferromanganese crusts from Dirck Hartog Ridge (DHR) located central Perth Abyssal Plain (PAP), Indian Ocean. Additional geochemical data, crust age estimations and selected data on formation processes, according to rare earth elements (REE) contents, were presented in our initial paper [30] on this general topic. Detailed tectonic and petrological description of DHR, including dredging data, were published in Reference [31].

2. Geological Setting

The Perth Abyssal Plain (PAP) is a large structural underwater topographic feature located offshore southwest Australia (Figure 1). The PAP western margin is defined by Batavia and Gulden Draak knolls, which were conjugated to part of the northern Naturaliste Plateau and Bruce Rise, respectively [32]. The eastern border is the Western Australian Shelf. The northern margin is represented by two major plateaus—Zenith and Wallaby—while the southern border is more complicated, composed of the Broken Ridge and Naturaliste Plateau, divided by Naturaliste Fracture Zone and southernmost Diamantina Zone. The PAP started to form about 136 Ma when the seafloor between India, Australia and Antarctica separated by seafloor spreading [33].

The PAP is divided into Western and Eastern Perth Abyssal Plains by DHR—a linear bathymetric feature-oriented NNE–SSW, composed of a group of irregular ridges. The total DHR is over 600 km length and 30–50 km width, and extends to 2800 m and ~2200 m below sea level in the southern and northern parts, respectively. The DHR is dominated by alkali basalts, dolerites and gabbroic-type rocks [31]. Basalts recovered from the DHR are represented by highly altered alkaline type, showing traces of low-grade metamorphism (spilitization), being destroyed by hydrothermal fluid alteration [31]. According to the most recent research, the DHR might be a seamount chain of volcano-tectonic origin, associated with magmatic activity of the Kerguelen plume [31].

The PAP is influenced mainly by cold northward Western Australian Current (WAC) and warm southward Leeuwin Current (LC). Both currents are active most of the year, well oxygenated and nutrient-rich, with the strongest flow between March and April [34,35].

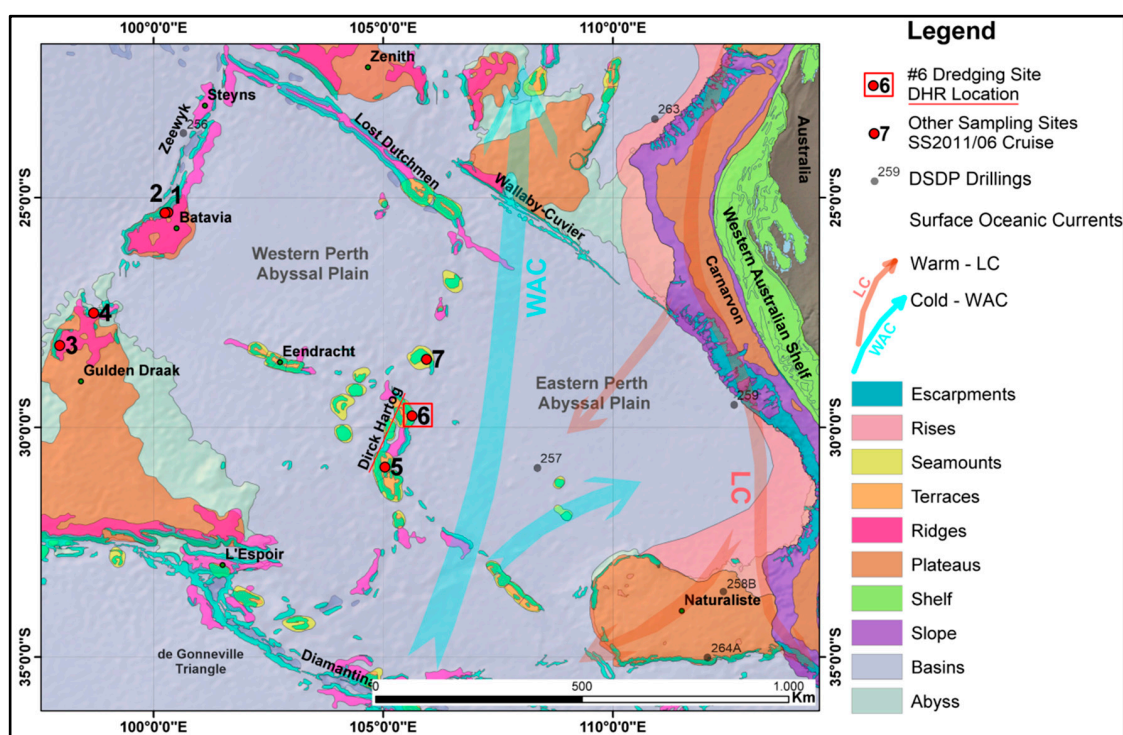


Figure 1. The DHR sampling sites location collected during cruise SS2011/06. Undersea feature names and borders follow General Bathymetric Chart of the Oceans (GEBCO Gazetteer) [36].

3. Materials and Methods

The ferromanganese crust samples from the DHR were collected in 2011 during SS2011/06 cruise aboard the Australian Marine National Facility vessel R/V Southern Surveyor. Three analyzed samples (DR6-9, DR6-10, DR6-11), were dredged from water depth 2680 m to 3345 m, along a 3-km long swath. On the surface of collected rock samples, several crusts of varying, generally low thickness (reaching

45 mm), have been identified. Only a few substrate rocks from the DHR were widely described prior to this study [31,32,37–39].

The representative sections of crusts and substrate rock samples were selected for analysis and divided into 10 subsamples (Table 1; Figure 2). Subsamples were ground in agate mortar and separated for X-ray Powder Diffraction (XRD), Energy Dispersive X-ray Fluorescence Spectrometry (XRF), Inductively Coupled Plasma Mass Spectrometry (ICP-MS), Differential Thermal Analysis (DTA) and Thermogravimetric Analysis (TGA). Grain mounts for Electron Probe Microanalysis (EPMA) were prepared from the solid parts. Selected geochemical data from XRF, ICP-MS (not presented here) and EPMA were published in Reference [30].

Table 1. General description of the DHR samples.

Id	Description
DR6-9	slightly weathered and crushed Fe-Mn crust; thickness up to 10 mm
DR6-9/2	yellowish-white mineral layer within the basalt-crust border zone; thickness up to 3 mm
DR6-9/3	medium weathered basalt
DR6-10/1	black-brownish minerals separated from the interior part of the thick (~45 mm) crust
DR6-10/2	highly weathered and slightly phosphatized basalt
DR6-10	black-brownish mineral mixture from the interior part of the crust
DR6-10/4	black-brownish mineral mixture from the interior part of the crust
DR6-11/1	black minerals (~2 mm thick) with a small white-yellowish dendrite-like forms (zeolites) separated from the upper part of the thick (~40 mm) crust
DR6-11/2	yellowish-brown phosphatized mineral mixture from the down part of the crust
DR6-11/3	black-brownish mineral mixture from the bottom part of the thick crust sample

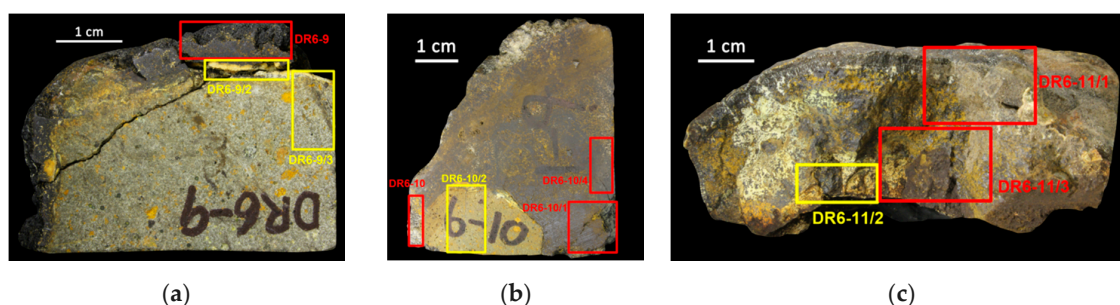


Figure 2. Representative cut sections of ferromanganese crusts from the DHR; (a) DR6-9; (b) DR6-10; (c) DR6-11. The red rectangles mark crusts subsamples selected for the XRD, DTA, XRF, ICP-MS and EPMA analyses. Yellow rectangles show places chosen for the substrate-crust alteration zone description, preparation of thin sections, XRD and EPMA.

The cut and thin sections of substrate rocks were polished and examined with Zeiss Axio Scope.A1 polarized light microscope, Ningbo CCD 5.1MP camera and ToupView photo software. The two subsamples of substrate basalt (DR6-9/3 and DR6-10/2), including white-yellowish mineral mixtures separated from crusts (DR6-9/2 and DR6-11/2), were analyzed using optical methods, XRD, XRF and EPMA.

The XRD mineralogy was studied by use of PANalytical Empyrean diffractometer, Royston, UK. The analytical conditions were: monochromatic CuK- α radiation at 35 kV and 30 mA, scans from 5–65° (2 θ), step size 0.024 (2 θ). The wide-angle detector (PIXcel 3D, Royston, UK) was used, with XRD data processed by Crystal Impact Match! 3 software and COD database [40].

The abundances of major (Si, Al, Fe, Mn, Ti, Cr, Ca, Na, K, Mg, P, S and Cl) and trace (Sr, Ba, Ni, Cu, Zn, Pb, V, As, Rb, Zr, Y and Nb) elements in the substrate basalts and basalt-crust border zone subsamples were determined by PANalytical Epsilon 3 EDXRF spectrometer (Royston, UK), equipped with SDD (silicon drift detector) and ceramic X-ray tube (50 kV, 9 W). Analysis was performed in helium

atmosphere, using pressed pellet method, three minutes counting time per sample and standard-less OMNIAN software.

The DTA and TGA were performed using MOM Q-1500D Derivatograph (Budapest, Hungary) [41] with “Derywat” (Kraków, Poland) data acquisition system [42]. Three samples (DR6-10/1, DR6-11/1 and DR6-11/2) were analyzed to confirm XRD results and receive information about thermal stability, oxygenation state, thermal weight loss and decomposition nature. Powdered crust samples (800 mg each) were placed in alundum crucibles. Al₂O₃ was used as a reference material. Samples were heated linearly from 20 °C to 1000 °C, in open-air atmosphere, and rate of 10 °C/min. The samples in the oven were covered with a glass cup for better heat dispersion. The TG, DTG and TA curves were registered, smoothed, aligned and leveled to an empty oven standard.

The chemical composition of minerals was determined using a JEOL SuperProbe JXA-8230 (Tokyo, Japan) EPMA at the Laboratory of Critical Elements, AGH University of Science and Technology, Kraków. The EPMA was operated in the wavelength-dispersion mode, at accelerating voltage of 15 kV and probe current of 20 nA. Focused beam with 1 µm diameter was used for manganese oxides, 3–5 µm for apatite and aluminosilicates, counting time of 20 s on peak and 10 s on both (+) and (–) backgrounds were applied. The following standards, lines and crystals were used for Fe-Mn oxyhydroxides: albite (SiKα, TAP; AlKα, TAP; NaKα, TAPH), tugtupite (ClKα, PETJ), barite (BaLα, PETJ), diopside (CaKα, PETJ; MgKα, TAPH), fayalite (FeKα, LIF), rhodonite (MnKα, LIF), rutile (TiKα, PETH), YPO₄ (PKα, PETH), Co (CoKα, LIFH), NiO (NiKα, LIFH), cuprite (CuKα, LIFH), willemite (ZnKα, LIFH), sanidine (KKα, PETL), celestine (SrLα, PETL), anhydrite (SKα, PETJ), crocoite (PbMα, PETH), Ti(Br,I) (TIMα, PETH) and GaAs (AsLα, TAPH); for aluminosilicates: albite (SiKα, TAP; AlKα, TAP; NaKα, TAPH), tugtupite (ClKα, PETJ), diopside (CaKα, PETJ; MgKα, TAPH), fayalite (FeKα, LIF), rhodonite (MnKα, LIFL), rutile (TiKα, PETH), YPO₄ (PKα, PETH), orthoclase (KKα, PETL), Cr₂O₃ (CrKα, LIFH); for phosphate minerals: albite (SiKα, TAP; AlKα, TAP; NaKα, TAPH), tugtupite (ClKα, PETL), barite (BaLα, PETJ; SKα, PETJ), diopside (MgKα, TAPH), fluoroapatite (CaKα, PETJ; PKα, PETH), hematite (FeKα, LIF), rhodonite (MnKα, LIF), willemite (ZnKα, LIFH), orthoclase (KKα, PETL), celestine (SrLα, PETJ), crocoite (PbMα, PETL), YPO₄ (YLα, PETJ), rutile (TiKα, PETH), CePO₄ (CeLα, LIFH), PrPO₄ (PrLβ, LIFH), GdPO₄ (GdLβ, LIFH), LaPO₄ (LaLα, LIFL), SmPO₄ (SmLα, LIFL), NdPO₄ (NdLα, LIFL) and GaAs (AsLα, TAPH). Data were corrected using ZAF procedure (Z—stopping power, back-scattering factor and X-ray production power; absorption—A; fluorescence—F autocorrection).

The results of REE content in the phosphate minerals were normalized to Post Archean Australian Sedimentary Rocks (PAAS), according to Reference [43].

4. Results

4.1. General Samples Description

The substrate rocks were identified as highly altered basalts. The texture of analyzed samples was phaneritic and porphyry, intergranular, needle-like, in some parts with small veins and vesicles up to 0.7–0.8 mm diameter, also directional and fluidic (Figure 3a,b). Major traces of weathering were visible, especially within the basalt-crust border zone. Vesicles were filled with celadonite, zeolites and small amounts of chalcedony. Plagioclases were dominated by bytownite-labradorite-andesine series, showing typical lamellar polysynthetic twinnings and extensive peritization. Additionally, some minor K-feldspar (orthoclase-sanidine) and albite phenocrysts were identified in the basalt matrix. Samples showed intensive pyroxene decomposition, with remnants of Fe and Cr-rich spinels and other dispersed non-identified non-opaque oxide minerals (Figure 3c,d). Some grains were identified in EPMA as a pseudobrookite and Mg-chromite. The small olivine remnants were completely decomposed to ‘iddingsite’.

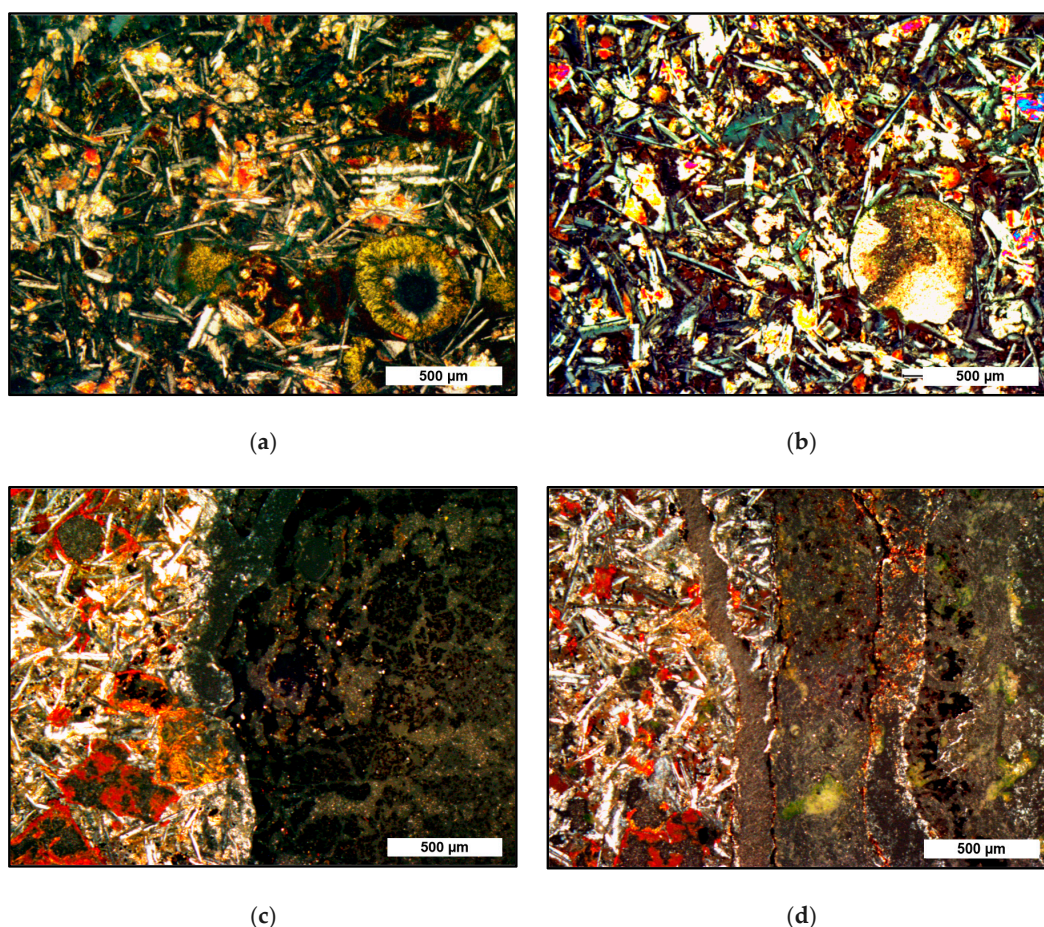


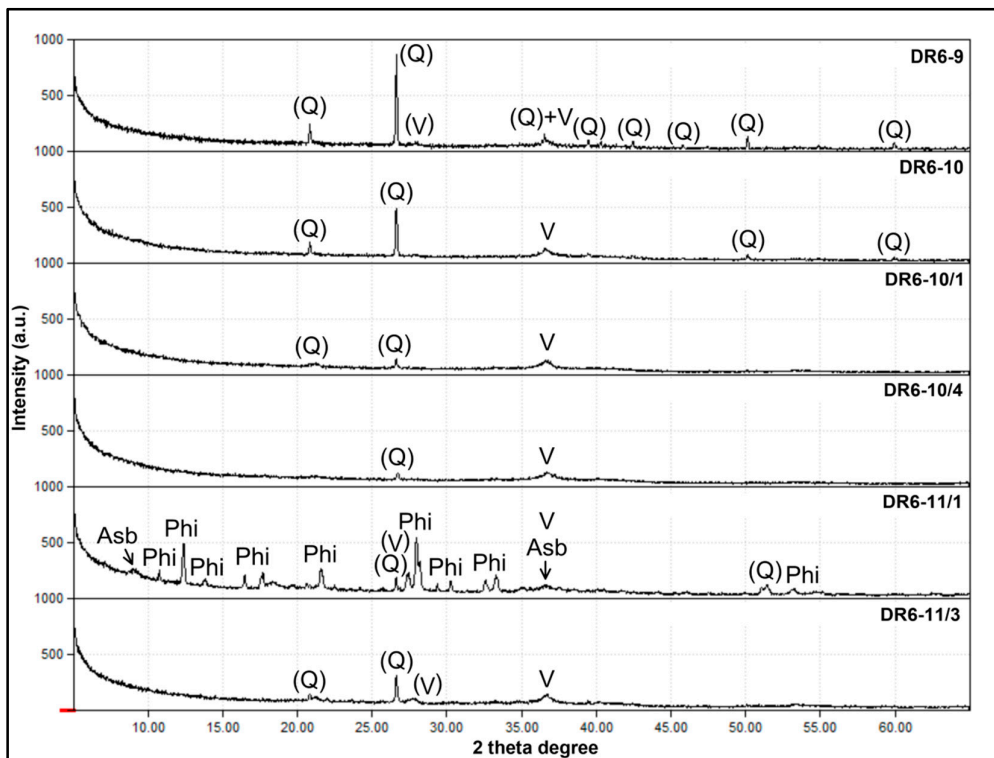
Figure 3. Representative transmitted light photos of the DR-9 sample; basalt interior (a), (b) and basalt-crust alteration zone (c), (d): (a) several plagioclase twinnings, small pyroxenes and vesicle filled with fibrous-like green celadonite; black non-opaque minerals were identified in EPMA as Fe-Cr rich spinels and pseudobrookite; (b) porphyrous, intergranular, needle-like texture with visible plagioclases, pyroxenes, non-opaque minerals and vesicle filled with chalcedony; (c) plagioclase twinnings with altered pyroxenes (red zones) and dispersed non-opaque minerals; starting from centre to right—the colomorphs complex composed of Fe-Mn oxyhydroxides and greyish Fe-rich clay minerals; (d) several plagioclase twinnings with altered pyroxenes and small veinlets filled-up with the mixture of clay minerals (Fe-smectite, nontronite), green authigenic hydroxyapatite and glauconite; visible on the right—black colomorphs and patches of Fe-Mn oxyhydroxides.

Substrate rock was covered by a thin layer of weathering products, being a mixture of amorphous hydroxyapatite, glauconite, clay minerals and a small amount of initial Fe-Mn oxyhydroxides. Visible clay fillings were often massive, patchy or fibrous in the texture (i.e., “flower-like” aggregates) (Figure 3a,d).

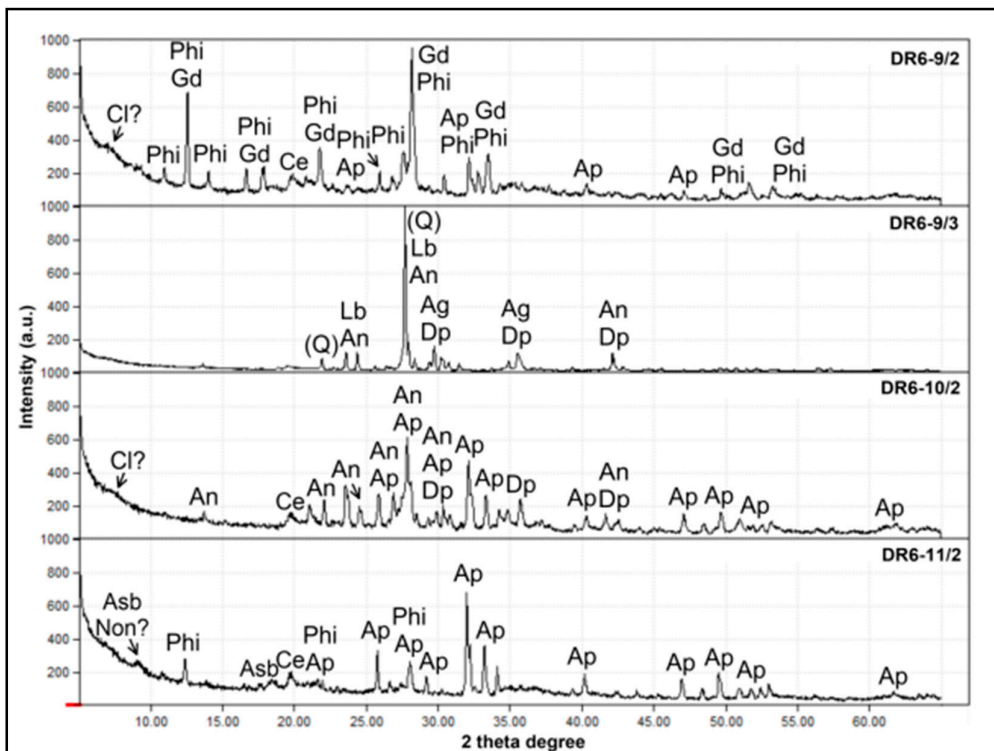
4.2. EDXRD

Described crusts were mineralogically dominated by low-crystalline Fe-Mn oxyhydroxides, mainly vernadite, with less asbolane. Due to low amount and crystallinity, the presence of ferrihydrite was confirmed only by EPMA.

The low-crystalline Fe-Mn bearing oxyhydroxides in type of vernadite show first broad asymmetric flat peak extreme around 2.46–2.44 Å and second smaller one ~1.42 Å. Due to the short range of prepared diffractograms the 1.42 Å peak was not visible, however presence of vernadite may be confirmed by weak 3.16 Å and 2.13 Å positions. Low crystalline asbolane was indicated by low broad reflections at 9.62–9.58 Å, 4.80–4.78 Å and 2.46–2.44 Å (Figure 4a,b).



(a)



(b)

Figure 4. Representative powder diffractograms of the crust samples from the DHR (a and b): (Q)—quartz; Fe-Mn oxyhydroxides: V—vernadite, Asb—asbolane; zeolites: Phi—phillipsite, Gd—gismondite; clay minerals: Cl—non-identified clay minerals, Non—nontronite, Ce—celadonite; phosphates: Ap—apatite (hydroxyapatite); other silicates: Dp—diopside, Ag—augite; plagioclases: Lb—labradorite, An—andesine.

Additionally, zeolites and phosphates were recognized as major crust phases. Presence of the Na-Ca zeolites—phillipsite and minor gismondite—was confirmed in the basalt-crust border zone. Zeolite in type of Na-phillipsite [44,45] was revealed in the subsamples DR6-11/1 and DR6-9/2 (reflections at 3.18 Å, 7.12 Å and 4.10–4.08 Å) (Figure 4a,b). Zeolites were identified mainly in mixtures with apatite and clay minerals. Apatite showed diagnostic 2.80 Å, 2.70 Å and 3.44 Å reflections [46,47] and was detected in DR6-11/2 and DR6-10/2 subsamples.

In the crust's basalt substrate, subsample DR6-9/3, presence of medium plagioclase—labradorite and andesine was indicated (Figure 4b), showing several diagnostic peaks around 4.06–4.05 Å, 3.78–3.76 Å, 3.64 Å, 3.37 Å, 3.20–3.18 Å and in the lower angles [48,49].

Identified Ca-Mg rich pyroxenes, in type of diopside and augite, showed diagnostic reflections at 2.89–2.99 Å and 2.51–2.56 Å [50,51] (Figure 4b).

Some trace broad reflections in high angles (d around 14 and 10 Å) shall be interpreted as clay mineral admixtures, mainly nontronite, celadonite or chlorite (Figure 4b) [52].

4.3. XRF

According to chemical bulk XRF analysis of the substrate rocks (DR6-9/2, DR6-10/2), the basalt samples were medium to high alkaline type showing 1.32 to 4.78 wt. % of K₂O and 38 to 43 wt. % of SiO₂ [53]. The Nb/Y and Zr/Ti values were 0.022 to 0.055 and 0.007 to 0.008, respectively, which is typical for sub-alkaline to alkaline basalt series [54]. According to Reference [55], analyzed basalts were Fe-dominated type, with FeO_t/(FeO_t+MgO) ratio in range of 0.82 to 0.93. The Zr/Y ratio from 0.26 to 0.54 and Ti/Y from 38 to 70 are typical for the plate margin basalts, suggesting oceanic source of magma [56,57]. High phosphorus content (0.22 to 3.50 wt. % of P₂O₅) and TiO₂ ~2.0 wt. %, indicated partial material acquisition from the island arc sources [58]. Basalts were low sulphated, showing CaO contents in range of 13.23 to 17.06 wt. %. The total content of Ni, Cu, Zn and Pb was >1000 ppm. Amount of vanadium was intermediate reaching 101 ppm. Basalts showed REE incorporation, mainly Y (181–314 ppm).

Subsamples being mixture of hydroxyapatite, clay minerals and zeolites (DR6-9/2, DR6-11/2) showed highly variable chemical composition: SiO₂ (25.91 to 44.66 wt. %), Al₂O₃ (8.89–12.00 wt. %), high FeO_t (~17.6 wt. %) and MnO contents (5.61 to 11.30 wt. %). Subsample with zeolites domination (DR6-9/2) indicated lower TiO₂ (0.95 wt. %), CaO (7.61 wt. %), P₂O₅ (1.73 wt. %) and higher K₂O (4.50 wt. %) and Na₂O (1.83 wt. %) contents, compared to the phosphatized crusts interior (DR6-11/2). Apatite dominated crusts interior was depleted with SiO₂, Al₂O₃ (25.91 and 8.89 wt. %, respectively), Na₂O and K₂O (0.75 and 1.97 wt. %, respectively), showing however higher CaO (21.20 wt. %), MnO (11.30 wt. %), P₂O₅ (5.19 wt. %), TiO₂ (2.17 wt. %) and MgO (2.51 wt. %) contents. DR6-11/2 subsample indicated also the highest contents of S (0.40%), Cl⁻ (0.28), Sr and Ba (>2000 ppm), As (40 ppm), V (202 ppm), Zr (235 ppm) and Y (1220 ppm). The Σ(Ni, Cu, Zn, Pb) of zeolitized and phosphatized samples is high, >8000 ppm and >10,500 ppm, respectively. Complete chemical results of EDXRF bulk samples analysis are presented in the Table 2.

4.4. DTA and TGA

The DTA and TGA curves of analyzed DHR subsamples showed one intensive endothermal (A) and one weak exothermal effect (B), in some parts of the curves—due to the polymineral samples composition—some slight variation in their shapes. The exothermal effect was dominant during analysis of all samples. The few stage dehydration-dehydroxylation in lower temperatures (<530 °C) and reduction of Fe-Mn bearing phases was observed (>530 °C). Large initial weight lost confirms large amount of water incorporated into the structure of water bearing minerals (mainly Fe-Mn oxyhydroxides, zeolites, hydroxyapatite and clay minerals). Thermograms of each analyzed sample are shown on Figure 5. Formation of new high temperature (>850 °C) mineral phases in the DR6-11/3 subsample was confirmed by additional XRD heating analysis (up to 1000 °C), indicating presence of Fe- and Mn-rich, such as braunite, jacobsonite, hematite, Ca-ferrite and Mn-Fe(III) oxide (Figure 5d).

Table 2. EDXRF chemical results of the bulk samples from the DHR.

Sample Description	Unit	DR6-9/3	DR6-10/2	DR6-9/2	DR6-11/2
		Medium Weathered Basalt	Highly Weathered and Slightly Phosphatized Basalt	Yellowish-White Zeolitized Mineral Mixture Basalt-Crust Border Zone	Yellowish-Brown Phosphatized Mineral Mixture Crusts Interior
SiO ₂	[wt. %]	43.25	38.14	44.66	25.91
Al ₂ O ₃		15.00	12.64	12.00	8.89
FeO ¹		18.91	18.35	17.60	17.64
MnO		0.43	0.51	5.61	11.30
TiO ₂		2.00	2.10	0.95	2.17
Cr ₂ O ₃		0.12	0.10	0.01	-
CaO		13.23	17.06	7.61	21.20
Na ₂ O		1.17	0.88	1.83	0.75
K ₂ O		1.32	4.78	4.50	1.97
MgO		3.90	1.29	2.28	2.51
P ₂ O ₅		0.22	3.50	1.73	5.19
S		0.02	0.11	0.19	0.40
Cl ⁻		0.06	0.06	0.06	0.28
Sr	[ppm]	292	608	371	1150
Ba		437	-	124	890
Ni		438	304	4522	7061
Cu		292	456	2708	1911
Zn		263	304	731	1054
Pb		73	76	166	489
V		101	101	134	202
As		0	23	-	40
Rb		27	55	27	25
Zr		81	96	110	235
Y		314	181	31	1220
Nb		7	10	-	-
Nb/Y		0.022	0.055	-	-
Zr/Y		0.26	0.54	3.55	0.19
Ti/Y		38.09	69.64	184.26	10.65
Zr/Ti		0.007	0.008	0.019	0.018

¹ Total iron calculated as FeO + Fe₂O₃.

The total weight loss in the DR6-10/1 subsample was extremely high and equal to 67.4%. The DTA and TGA curves are simple in their shape, showing intensive endothermal dehydration effect of vernadite and some minor phases (phillipsite, nontronite), with maximum in 196 °C (Figure 5a). Less intensive exothermal effect visible between 350–400 °C needs to be considered as a “protohematite” formation from iron gels. Other low exothermal effects, observed between 400–500 °C and 650–700 °C, are devoted to oxidation of Fe-bearing phases [59]. In the higher temperature (>810 °C) some further dehydroxylation and decomposition occurs.

The total weight loss in the DR6-11/1 subsample was 45.5% (Figure 5b). Thermal curves show mainly effects of phillipsite dehydration, with maximum endothermic effect in 181 °C and typical double effect of 12 mole loss of zeolitic and crystalline water occurring in 210–250 °C. Above 435 °C, the phillipsite structure is destroyed. Observed thermal effect was “masked” by dehydration of vernadite, asbolane and other water bearing phases (nontronite, celadonite, hydroxyapatite, Fe-gels). Nontronite and asbolane dehydroxylation was visible around 440–450 °C. Mn⁴⁺ reduction to the Mn³⁺ state is visible through the entire DTA curve. Intensive and “flat” exothermal effect above 450 °C was probably connected with decomposition and recrystallization of Fe-rich minerals. In temperatures higher than 880 °C, further decomposition takes place [59].

The total weight loss in the DR6-11/2 subsample was 56.9%. Endothermal reaction started immediately after heating and lasted until 380 °C. The maximum intensity was observed around 180–190 °C. In this temperatures phillipsite starts to lose zeolitic and crystalline water. Above 450 °C structure is destroyed and formation of aluminosilicates occurs. Additionally, the reaction of water and CO₂ loss in hydroxyapatite takes place [60]. Mentioned effects are masked by intensive dehydroxylation of vernadite, nontronite and celadonite [61].

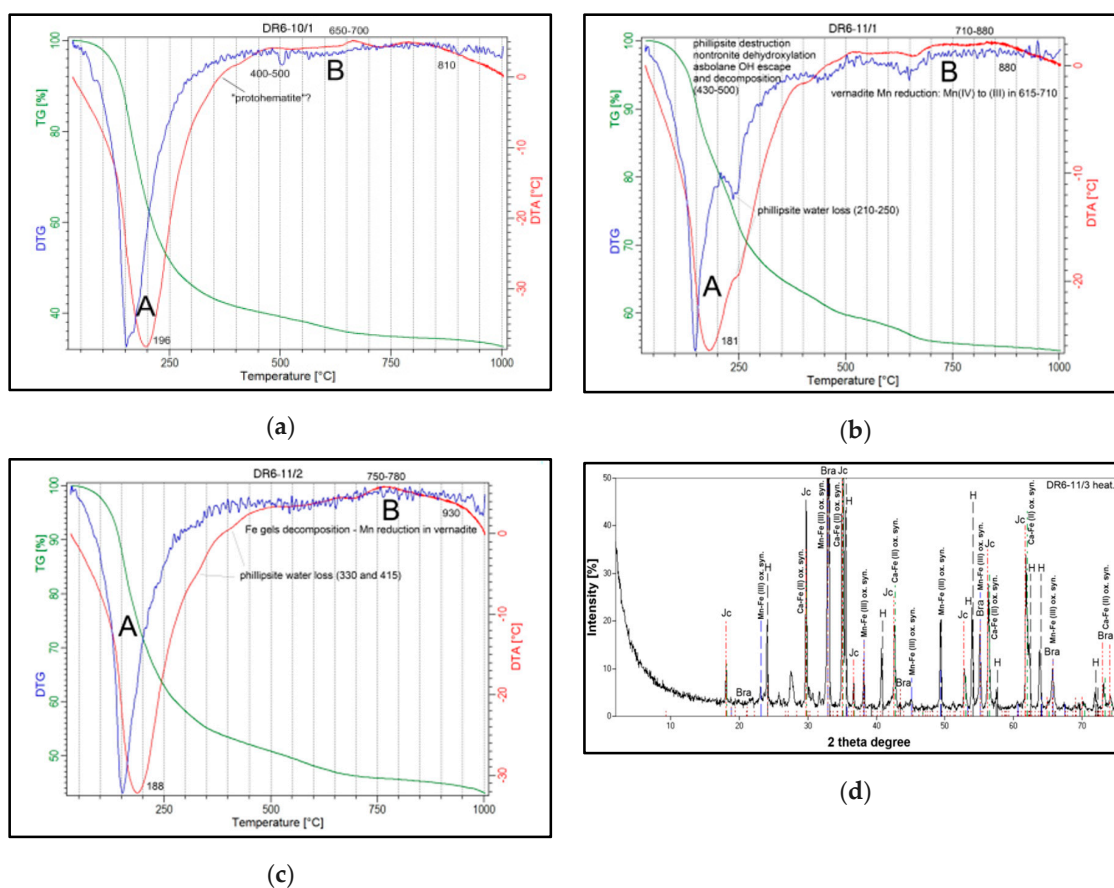


Figure 5. Representative DTA and TGA curves of the bulk crust samples from the DHR: (a) DR6-10/1; dehydration of vernadite and minor iron gels (feroxyhyte-ferrihydrite); B-wide exothermal decomposition of vernadite and Fe-rich gels; manganese reduction in vernadite (3^+ to 2^+); synthesis of the new mineral phases; (b) DR6-11/1; A-dehydration and dehydroxylation of phillipsite, vernadite, asbolane and other phases (hydroxyapatite, nontronite, celadonite), structure destruction in phillipsite and asbolane; nontronite dehydroxylation; B-exothermal decomposition of Fe-gels and Mn reduction in vernadite; low intensive dehydroxylation of phyllosilicates; >880 °C synthesis of the new mineral phases; (c) DR6-11/2; A-dehydration and dehydroxylation of vernadite, asbolane, hydroxyapatite, phillipsite, nontronite and celadonite; carbon dioxide loss in hydroxyapatite; B-exothermal decomposition of Fe-gels and Mn reduction in vernadite; further dehydroxylation of phyllosilicates; >950 °C synthesis of the new mineral phases; (d) XRD diffractogram of the heated DR6-11/3 subsample shows presence of synthetic braunite, jacobsonite, hematite, Ca-ferrite and Mn-Fe(III) oxide.

The interior part of two subsamples (DR6-10/1 and DR6-11/2), compared to DR6-11/1, exhibited higher content of water, caused mainly by more intensive dehydration of the crust surface in the open-air atmosphere, higher porosity of internal structure or different redox potential, affecting internal ability of incorporating OH^- groups.

4.5. EPMA

More than 200 EPMA analyses performed on the DHR crust samples revealed the presence of a few types and subtypes of Fe-Mn rich oxyhydroxides, forming several colomorph structures, being already described in Reference [30].

Several laminae of metal-rich vernadite, asbolane and metal depleted ferroxyhyte-ferrihydrite were analyzed. In general, vernadite and asbolane layers show intensive incorporation of metals such as Cu, Ni, Co and Ti. High contents of REE were confirmed only in the Ca-hydroxyapatite. Low concentrations of the REE were discovered in the alteration zone, mainly in the slightly phosphatized mixtures of clay minerals (nontronite, glauconite, celadonite) and zeolites. The REE traces were recognized also in the substrate basalt minerals (plagioclases, pyroxenes), including clay and zeolite fillings of vesicles and veinlets. The EPMA revealed depletion of the REE in the structure of analyzed Fe-Mn oxyhydroxides.

According to the DHR substrate basalt analysis, the feldspar group is represented mainly with bytownite-labradorite series, with minor phenocryst of alkali rich albite and orthoclase-sanidine. Feldspars general formula is $A_1T_2Si_2O_8$, showing several occupying the *A* sites (i.e., Na^{2+} , K^+ , Ca^{2+} , Sr^{2+} , Ba^{2+} , Rb^+ , Pb^{2+} and REE^{3+}) and *T* sites (i.e., Si^{4+} , Al^{3+} , Fe^{3+}).

Calculated feldspar end-members in the DHR samples were, respectively: $An_{47.64} Ab_{19.30} Or_{33.06}$ for bytownite, $An_{49.93} Ab_{47.97} Or_{2.10}$ for labradorite, $An_{2.65} Ab_{94.69} Or_{2.66}$ for albite and $An_{0.10} Ab_{0.47} Or_{99.43}$ for orthoclase-sanidine. Only albite showed some slight cation deficiency at the *A* sites. Plagioclases were well developed, with several twinnings, zoned and partially perthitized, showing several solid inclusions of pyroxene and oxide Ti-rich minerals (mainly pseudobrookite). Additionally, highly weathered, decomposed feldspar remnants were identified in the basalt-crust alteration zone (Figure 4). Bytownite-labradorite end-members show some traces of yttrium content (28–189 ppm), indicating also some structural impurities of Ti, Fe, Cr, Mn and Cl (usually <1 wt. %).

The pyroxene group in the DHR samples is represented mainly by augite, with minor diopside and ferrosilite (Figure 4b). Pyroxenes are silicates built from SiO_3 linked with SiO_4 tetrahedra. Generally, small amounts of Si are replaced by Al and other small cations. The simplified chemical formula for all pyroxenes is $M_2M_1T_2O_6$, where *M*₂ refers to cations in a generally distorted octahedral coordination, *M*₁ to cations in a regular octahedral coordination and *T* to tetrahedrally coordinated cations [62].

Calculated pyroxene end-members in the DHR samples were: augite ($Wo_{24.85} En_{30.32} Fs_{23.83} Ae_{21.00}$), diopside ($Wo_{40.15} En_{48.62} Fs_{10.41} Ae_{0.82}$), ferrosilite ($Wo_{2.53} En_{29.33} Fs_{63.56} Ae_{4.58}$). Augite, and especially ferrosilite, indicate cation deficiency at the *M*₂ sites, mostly of Fe^{3+} . Diopside showed Cr impurities (up to 0.69 wt. %) and augite some traces of Y (<126 ppm). The highest Ti contents were measured in ferrosilite (mean 1.55 wt. %) and lowest in augite (~0.25 wt. %). The mean Mg and Ca contents (all in wt. %) were, respectively: 10.21 and 13.92 for diopside, 7.70 and 6.27 for augite, 4.08 and 0.35 for ferrosilite. Chlorine in pyroxene was low (<0.44 wt. %). The calculated Si/Al ratio was highest for the diopside (16.11) and lowest for ferrosilite (3.28).

Recognized and analyzed in EPMA were also some minor oxides, represented by pseudobrookite, Mg-chromite and zircon.

Pseudobrookite is a rare, iron-rich titanium oxide mineral with the formula of $(Fe^{3+}, Fe^{2+})_2(Ti, Fe^{2+})O_5$ and is an indicator for pneumatolitic processes in Ti-rich rocks, i.e., in vesicular basalts. A few grains of pseudobrookite were found as solid inclusions in feldspars (Figure 6a) and in association with Mg-chromite and pyroxenes, especially strongly altered augite. Mean Fe_{tot} and Ti contents in pseudobrookite are, respectively 53.05 and 13.60 wt. %. Some non-significant amounts of chemical impurities were detected (Al, Mg, Ba), also with metal traces (Mn, Ni, Cu, Co, Zn, Pb and Tl).

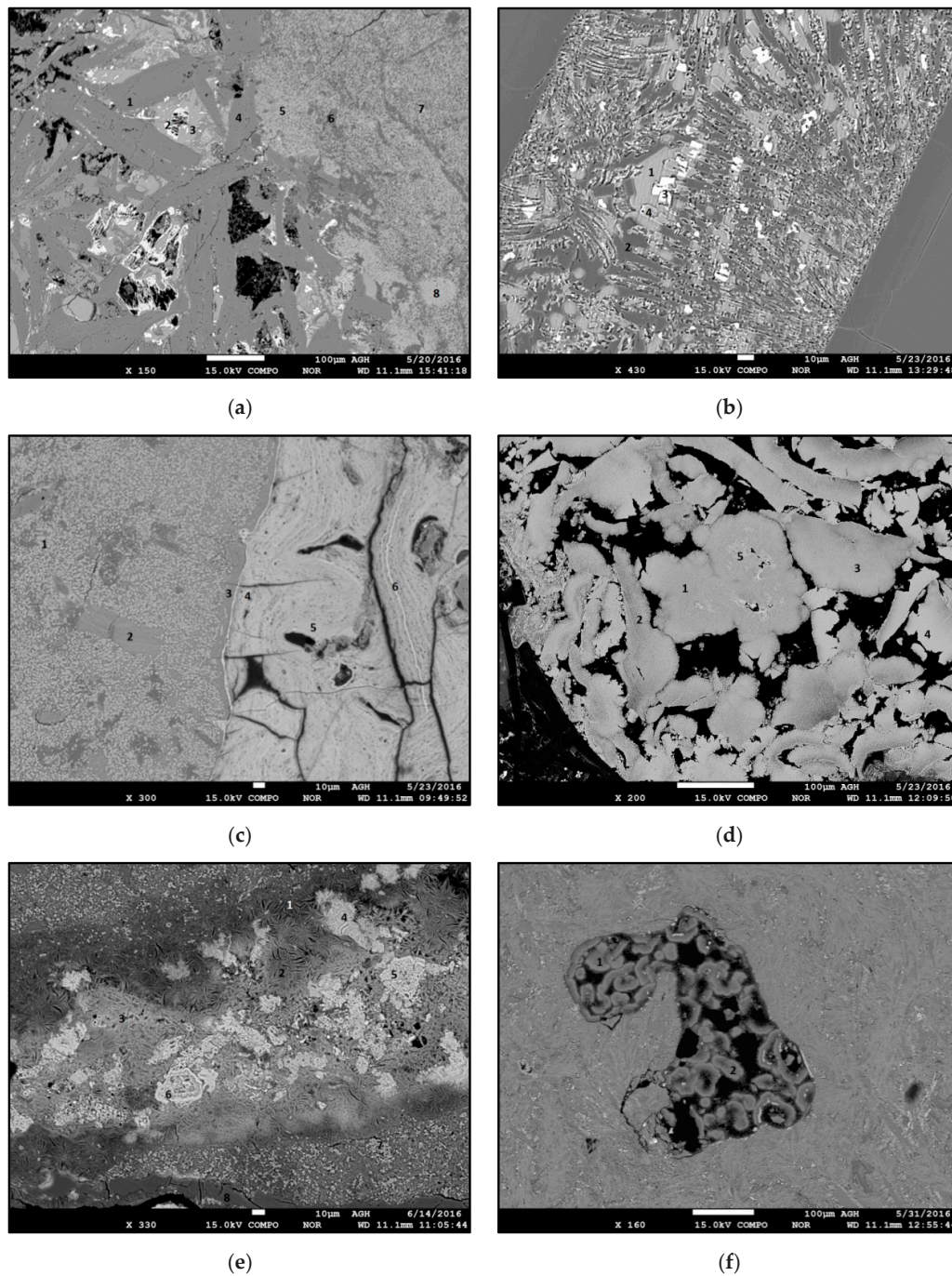


Figure 6. Representative EPMA images of DHR basalts and substrate-crust border zone: (a) several plagioclase twinnings (1, 4), hydroxyapatite (3, 5, 7, 8), remnants of pyroxenes (6) and pseudobrookite; (b) part of pertitized, zoned plagioclase phenocryst (1, 2) with remnants of automorph pyroxene (4) (ferrosilite) and pseudobrookite (3); (c) transition zone with graspy basalt texture and pyroxene remnants (2); amorphous hydroxyapatite with small admixture of Zn, Fe, REE and depleted with F^- (1); phyllosilicate substrate coating developed as a weathering product (3) (celadonite-ferroceladonite or Fe-saponite?); colomorphs with laminae of asbolane (6) and vernadite (4, 5) with $>1.7\%$ Ti + Co and $\sim 1.0\%$ Ni + Cu + Zn; (d) worm-like phyllosilicate filings from basalts vesicle (nontronite and celadonite); (e) weathered basalts vesicule filled-up with the flower-like radial porous clusters of Fe-chlorites, celadonite and nontronite (showing higher contents Cr and Y); small intergrowth ($\sim 40\ \mu\text{m}$) of Ni-asbolane (4) and Ni-Cu asbolane (~ 40 to $50\ \mu\text{m}$) (5, 6); (7) hydroxyapatite depleted with F (0.5%) and REE (Y + La) (0.5%); (8) small vein (10 to $20\ \mu\text{m}$) composed of zeolite (Na-K philipsite); (f) basalt vesicule filled-up with worm-like phyllosilicate mixture (ferroaluminoceladonite and nontronite).

Mg-chromite is a Fe-Mg rich oxide, classified in the spinel group, with general formula of $\text{MgCr}^{3+}_2\text{O}_4$. Iron is substituted mainly by variable amounts of Mg, and minor Al, V, Ti, Mn and others. Chromite spinels are often associated with seafloor basalts, being indicators of serpentinization processes, mostly low-silica initial metamorphism, Fe-oxidation and hydrolysis of mafic rocks.

Mg-rich spinels analyzed in the substrate basalts from DHR showed high Cr and Fe contents (27.25 and 18.49 wt. %, respectively; Cr/Fe ratio 1.47). Vanadium content was 0.11 wt. %. Admixtures of Ni, Co, Zn (sum <0.20 wt. %), Ti, Mn, Si and Ca ($\Sigma \sim 0.8$ wt. %) are generally low.

Zircon is an important accessory silicate mineral, being associated with all geological environments, with the general chemical formula of $(\text{Zr}_{1-y}, \text{REE}_y)(\text{SiO}_4)_{1-x}(\text{OH})_{4x-y}$. Zircon shows high contents of high field strength incompatible elements (so-called HFE: Zr, Hf, Nb, Ta, REE^{3+} , Th and U), in some cases with impurities of alkali and alkaline metals.

Analyzed zircon grains from the DHR basalts showed mean Zr content of 48.28 wt. %, Th over U domination (642 to 335 ppm, respectively; Th/U ratio 1.94) and large amount of REE (1.69 wt. %), mainly Y (1.0 wt. %) and other HREE ($\Sigma \text{Yb, Er, Lu} > 0.5$ wt. %). The mean hafnium content was 0.83 wt. %. Some impurities of Fe, Ti and Ca were also present (<1.0 wt. %).

According to the chemical analysis of substrate-crust border zone, phosphate minerals were represented by Ca-hydroxyfluorapatite (CHFA) with general formula of $\text{Ca}_5(\text{PO}_4, \text{CO}_3)_3(\text{OH})$. The CHFA showed mean 36.7 wt. % of calcium and 13.51 wt. % phosphorus content. Several admixtures and structural impurities of Si, Al ($\Sigma_{\text{Si} + \text{Al}} = 1.96$ wt. %), Ba, Sr ($\Sigma_{\text{Ba} + \text{Sr}} = 470$ ppm), Mg, Na, K (total sum of 1.01 wt. %), Fe, Mn ($\Sigma_{\text{Fe} + \text{Mn}} = 0.93$ wt. %), Ti (500 ppm), Ni, Cu, Zn, Pb (total sum of 0.12 wt. %) and sulphur (0.44 wt. %) were detected. The mean fluorine and chlorine contents were 1.22 and 0.03 wt. %, respectively. The REE were dominated by Y, La and Nd. The mean REE was 0.57 wt. %. Analyzed apatites indicated some cation excess at the Z sites (+0.279) and deficiency at B sites (−0.185).

According to the chemical calculations and empirical formulas of Fe-Mn oxyhydroxides (Appendices A and B, Tables A1 and A2), a few general assumptions may be defined. Identified asbolanes showed lower Ti amounts and higher Al, Mg, K, Na, Zn comparing to vernadites. The manganese content in asbolanes varied from 36 to 41 wt. %. The mean cobalt and nickel contents were also high, especially in the Ni-Co-(Cu) subtype and reach 0.70 and 4.11 wt. %, respectively. A bit lower mean values of Co and Ni were observed in Cu-rich subtype, where $\text{Cu} > \text{Co}$ (Cu mean content 0.84 wt. %). Asbolane lamellae were thin, usually from 2–5 to 15–20 μm (Figure 7). Mean iron content and Mn substitution were also low. The analyzed vernadite lamellae were usually in the Mn-(Fe) type, indicating greater Si, Ba, Sr, Ca, Pb, S and Cl^- contents. All vernadites showed lesser amount of H_2O^- , compared to asbolanes. In the Mn-dominated subtype $\text{Co} > \text{Ni} > \text{Cu}$ was observed. The highest silica and phosphorus contents were strictly connected with the higher Fe amount and were indicated in the Fe-(Mn) vernadite and mixture of non-defined feroxyhyte/ferrihydrite. Fe-rich oxyhydroxides in type of iron gels are usually depleted with Ca, Na, K and metals such as Ni, Co or Cu. In the few EPMA points of analyzed Fe-rich minerals some greater amount of Ti was indicated (mean 4.83 wt. %), probably as a Ti/Fe substitution in the crystalline lattice. Fillings of Ti-rich feroxyhyte and ferrihydrite showed usually higher contents of Ba, Cl^- and Mg, but with the lowest values of incorporated structural water.

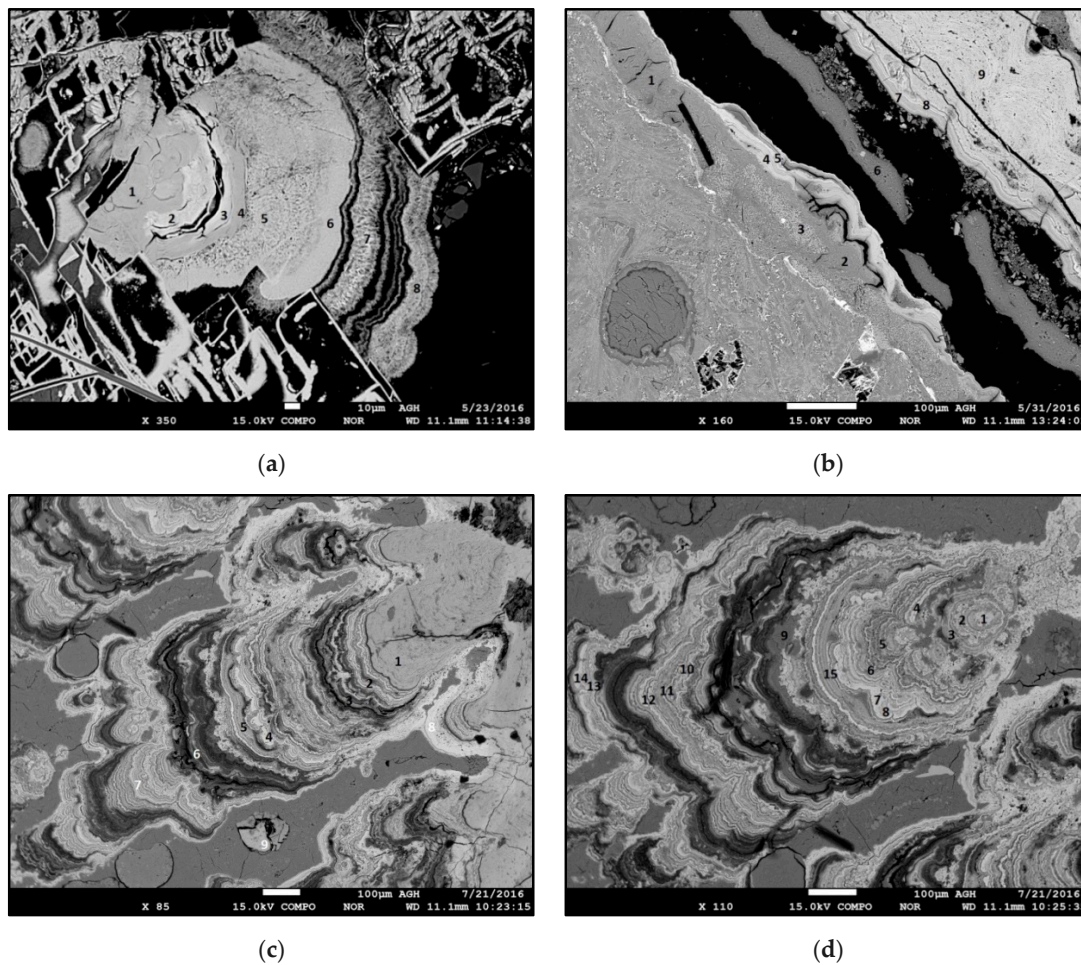


Figure 7. Representative EPMA images of DHR Fe-Mn crusts minerals: (a) (1, 3, 4) sequence of asbolane with high grade of Ni (6.2–7.3%); (2) Ni-Co asbolane showing >1.6% Co; uniform texture with change in (5) to more patchy and porous; (5) low-grade Ni-asbolane with higher Mn content 47% and low alkali content; (6) low-grade Ni-(Co) asbolane; (7) and (8) Ni-asbolane (or buserite) with fibrous texture and Ni content from 4.1 to 5.8; (b) basalt-crust transition zone with elongated coatings of phosphatized clay minerals (1, 2) (glaucanite, nontronite, traces of ferroaluminoceladonite) with intergrowths of hydroxyfluorapatite (3); “vein” in central part with remnant filling of nontronite, glaucanite and celadonite; (4, 5) Fe-rich colomorphs of Ti-rich feroxyhyte-ferrihydrite; (7, 8) lamellae (up to 5 µm) of vernadite; (9) massive vernadite with wavy and grainy texture and increased Ti content; (c) thick vernadite (1) with higher content of Co (>0.6%) and Ti (>1%); (2) Ni-Cu asbolane (~10 µm) with Ni (>3.5%), Cu (>1%), Zn (>0.5%) increased Mg content and depleted with P, Co and Ti; (3) Fe-chlorites depleted with metals; traces of alteration; (4) small lamellae of asbolane (~µm) with Ni + Cu + (Zn) content >4%; (5) mixed group of vernadite and asbolane, slightly depleted with metals; (6) asbolane with Ni + Cu + (Zn) content >5% and increased Mg content; (7) bright laminae of Mn-rich asbolane slightly depleted with metals and Mg; (8) asbolane depleted with metals (~2%); (9) crushed grain of non-identified Fe-Si-Ti rich mineral; (d) small aggregate-core (1) of Ni-(Cu) asbolane with amount of Ni + Cu + Zn (~4%) and increased Mg content; asbolane (2, 3) showing metal depletion down to 2.5%; asbolane (4) with high content of Ni + Cu + Zn (4.5%) and Mg, depleted with alkali metals; sequence of asbolane laminae (5–8) showing increase of Σ (Ni, Cu, Zn) content (>5%); zeolite (heulandite-clinoptilolite) layer (9) depleted with metals, Sr, Ba and Ca; being part of crushed-like alteration zone; Ni-Cu asbolane sequence (10–12) showing increase of metals content up to 5.2%; another sequence of Ni-Cu asbolane (13, 14) showing increased metal content; (15) mixed laminae of vernadite and asbolane; higher content of Ti + Co (~1.7%) in vernadite.

5. Discussion

5.1. Mineralogy of Ferromanganese Co-Rich Crusts

The Co-rich ferromanganese crusts are composed primarily of highly amorphous hydrated Fe-Mn minerals, mainly vernadite and ferrihydrite. Other mineral phases may include asbolane, ferrihydrite, todorokite, birnessite, busserite, manganite, psilomelane and goethite, i.e., [7,13]. Crusts are often phosphatized and show, in some cases, admixtures of detrital components [3]. Generally, chemical elements are associated with one or more of five phases in Fe-Mn crusts: vernadite, ferrihydrite, residual aluminosilicates, carbonate-fluoroapatite (CFA) and residual biogenic phases, e.g., [63]. The Co, Zn, Ni, Mg, Ba, and Tl are generally associated with vernadite; As, Bi, Cu, Cr, Mo, Nb, Pb, Te, Ti, Th, W, and Zr with ferrihydrite; Si, Al, K, Ti, Cr, Mg, Fe, Na, Sc, and Rb with several aluminosilicates; P, Ca, CO₂, Sr, and Y, with CFA (the measured CO₂ is bound as CO₃²⁺ in the CFA structure); presence of Ba, Sr, Ce, Cu, V, Ca, and Mg is connected with the residual biogenic phase, e.g., [29]. The REE, Y, Cu, Zn, and V can partition between the Fe and Mn phases.

Iron is the most widely distributed element and occurs intermixed in vernadite. The Fe is also the main constituent of ferrihydrite/ferrihydrite and occurs in several detrital minerals, such as pyroxenes, amphiboles, magnetite (and other spinels) and clay minerals. The CFA occurs only in the inner layers of thick crusts. In thin crusts and outer layers of thick crusts, calcium may be associated with vernadite, phosphorus with the FeO(OH) and both with biogenic residuum. Content of CFA-associated elements (P, Ca, Sr, and Y), as well as Te, Pt, Rh and Ir, generally increase with the crust thickness. In contrast, contents of elements associated with the detrital phase, usually decrease with increasing crust thickness [7]. Cobalt incorporation is an oxidation/reduction process between Co²⁺ and Mn⁴⁺/Mn³⁺ [64]. The hydrogenous crusts contain cobalt mostly in the oxidation state of +3 [65]. Significant Ni and Co substitution occurs due to similar geochemical behavior of both elements and ability to form complex and chelate compounds, especially in the case of ionic diameter similarity between Ni²⁺ and Mg²⁺ (6.9 vs. 6.6 nm). Nickel and cobalt are mobile, soluble and coexist in weathering processes, forming high concentrated Ni- and Co-rich clays in association with Fe-Mn oxyhydroxides, especially with asbolane [66] and Ni-vernadite. Both minerals adsorb heavy manganophilic metals (Co, Ni, Zn) and show extensive chemically active surface, indicating high ion-exchange capacity, which exceeds (in similar pH conditions) some clay minerals. Additionally, the high titanium contents and Al domination may be potential indicators of exceptional hydrogenous processes affecting crust formation [67]. Titanium is acquired primarily through sorption onto the Fe-oxyhydroxides, so high Ti concentration is related mainly to slower growth, which does not allow the time for significant sorption to occur [68].

The experimental model of oceanic bottom water solution, for vernadite and ferrihydrite rich Co-rich ferromanganese crusts, increases in the following order: (Li⁺ < Na⁺, K⁺ < Ca²⁺) < (Sr²⁺ < Ni²⁺ < Zn²⁺ < Cd²⁺ < Mn²⁺) < (Ba²⁺ < Pb²⁺ ≈ Co²⁺ < Cu²⁺) < Mo⁶⁺. Metal ions are absorbed directly from oceanic waters, immediately following the formation of manganese minerals, and continue during the entire period of crust growth. At the initial stage of manganese mineral formation, when structure is mostly disordered and marked by presence of maximal number of vacant sites (defects), sorptivity of the minerals is especially high. Activity processes are often independent of substrate type and crusts depth (600–3500 m), showing lesser desorption values with ageing.

Asbolane layers usually exhibit greater selectivity to Mn²⁺ and Ni²⁺ cations and lower to Mo⁶⁺ [27]. Dissolved manganese species, regardless of oxidizing conditions in solution, can co-precipitate on particles of rapidly forming X-ray amorphous (colloid) iron hydroxide or other surfaces, following the mechanism of heterogeneous hydrolysis. The process of joint precipitation of the iron and manganese oxyhydroxides has an autocatalytic character, which causes a tight intergrowing of ferruginous and manganese structures with formation of thin intercalated Mn- and Fe-rich layers, even at a micro level [23].

The X-ray reflection δ -MnO₂ (vernadite) and X-ray amorphous Fe oxyhydroxide FeO(OH) dominate in the crust mineral composition within 90–95% of crystalline phases. The remaining 5–10% are detrital minerals such as quartz, plagioclase, feldspar, pyroxenes and phillipsite. Thick crusts are usually phosphatized in the older layers and 30% of crystalline phases are usually CFA [2,13]. Phosphatization occurs often in several layers [69]. Iron and manganese dominate in the chemical composition of hydrogenetic crusts. The ratio of these two elements vary between 0.4 and 1.2, most often 0.7 ± 0.2 . The iron content in this type of crusts ranges from 12 to 26% with mean 21%.

5.1.1. Fe-Mn Oxyhydroxides

Hydrogenous crusts, as presented in this paper, are usually dominated by vernadite, showing in some cases presence of other low-crystalline Fe-Mn oxyhydroxides.

Vernadite (Mn⁴⁺,Fe³⁺,Ca,Na)(O,OH)₂·nH₂O is genetically mainly hydrogenous, highly disordered, randomly stratified nanocrystalline Fe- and Mn-bearing phylломanganate, with hexagonal layer symmetry and several diadochal constituents, mostly of Na, K, Ca, Mg and several metals such as Cu, Fe and Co [70,71]. Vernadite is the dominant mineral in crusts and nodules forming under oxidizing conditions, mainly by rapid oxidation of Mn²⁺ [72,73] and exhibits typical “grassy” forms. The so-called Fe-vernadite has a hybrid structure with coexisting Mn⁴⁺ and Fe³⁺ domains. Observed higher Fe substitution instead of Mn is typical of Fe-vernadite, which is more abundant in oxic environments, possibly due to higher resistance to reduction. Fe-vernadite need to be considered also as an early and unstable oxydogenesis product [74]. On the other hand, the Mn-dominated type of vernadite, is one of the most abundant and reactive Mn oxyhydroxides, especially in suboxic aqueous systems. Vacant [MnO₆]-octahedral sheets of Mn-(Fe) phylломanganates may contain several substitutions of lower valence cations (i.e., Mn³⁺, Ni²⁺, Cu²⁺, Zn²⁺ and Co³⁺) [75]. Metals can be incorporated above these vacancies or even between them. In the hydrogenetic oxic environments, Mn is speciated as a Fe-vernadite, showing intergrowths with feroxyhyte (δ -FeOOH) and monodispersed phylломanganate layers, having no interlayer of Mn-vernadite. In suboxic environments, which are dominated by diagenetic Fe-Mn rich crusts and nodules, Mn is speciated predominantly as Mn-rich 10 Å vernadite, which consists of random intergrowths and the transformation product todorokite [76]. Vernadite may be found separately also as a biogenic product of Mn-oxidizing bacteria, whereas the same mineral associated with ferrihydrite is produced abiotically via the heterogeneous oxidation of Mn²⁺_{aq} initially on ferrihydrite surfaces [77]. Vernadite may contain several mechanical admixtures or epitaxial intergrowths of other Fe-rich minerals, such as goethite and feroxyhyte. Fe-depleted vernadites, obtained from aqueous solutions of metal salts and natural marine environment, show tendency for transformation to asbolane-buserite over time, mainly under the influence of sorbed cations of Ni²⁺ and Co²⁺ [78].

Vernadite from the DHR shows low Mn/Fe ratio (~1.77). Average Ni + Cu + Co content equals to 1.37%, with Co domination. Crust samples show exceptionally high Ti contents (mean 1.23%, max 4.77%). Compared with other Fe-Mn oxyhydroxides identified in the EPMA, vernadite shows the highest Cl, S, Ba, Ca, Sr, P and Zn (Table A1, Figure 8). In samples from the DHR Fe-vernadite is dominant, showing several intergrowths with Ni and Ni-Co asbolane and feroxyhyte-ferrihydrite domains and in the analyzed area occurs in association with other Fe-Mn rich phases, quite similar to other crust regions (compare References [79,80]).

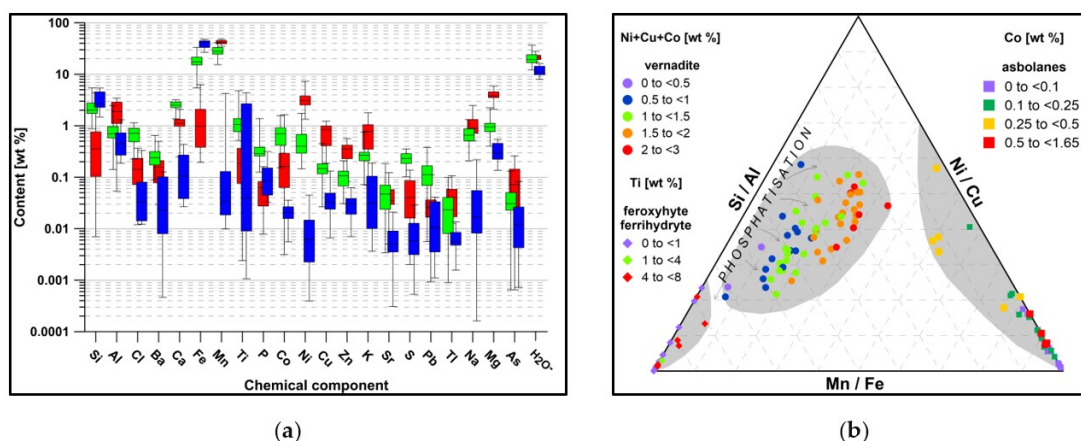


Figure 8. Chemical variability and classification of DHR Fe-Mn oxyhydroxides; (a) whisker plot shows chemical variability between elements in the identified Fe-Mn bearing phases; blue for feroxyhyte and ferrihydrite, red—asbolanes, green—vernadite; whiskers represent minimum and maximum values; black line in boxes is a mean value; H_2O^- calculated as rest from EPMA; (b) discrimination diagram of DHR crusts Fe-Mn bearing oxyhydroxides, according to Mn/Fe, Si/Al, Ni/Cu ratios and selected elements content (Ni + Cu + Co, Ti and Cu); gray areas represent fields of vernadite, asbolanes and feroxyhyte-ferrihydrite. Arrows indicate increase of phosphatization. All data from EPMA.

Asbolane $Mn^{4+}(O,OH)_2 \times (Co,Ni,Mg,Ca)_x(OH)_{2x} \times nH_2O$ is less dominant but a major concentrator of economically important elements, especially Ni and Co. Asbolane is mainly a product of the transformation of other manganese minerals, often being translated as diagenetic process. However, in some cases (NW-Pacific) asbolane could be formed directly by hydrogenetic processes [27] and may show hybrid forms, composed either only of octahedral layers (e.g., Co-Ni asbolane and Ni-asbolane) or of octahedral and tetrahedral layers alternating along the *c* axis (Co-asbolane). Ni^{2+} occurs mainly in the chemically bound form, as insular $Ni(OH)_2$ interlayers. Co-Ni asbolane is formed by layers of MnO_2 , $Ni(OH)_2$ and possible $CoOOH$ or $Co(OH)_3$ and may build intergrowths with busserite and other manganese oxyhydroxides [27,81]. Epitaxial asbolane growth, especially with Fe phases such as goethite or feroxyhyte, may be an indicator of undersaturation [82] or presence of some low-oxidation horizons. Asbolanes are often considered as initial for crust formation, being also the oldest part in the crust's age sequence. Some low-crystalline Fe-vernadite may undergo transformation into asbolane, mainly under the influence of adsorbed Co^{2+} cations [27]. Higher Co and Ti contents in asbolane suggests slower sorption and oxidation processes typical for hydrogenetic material [83].

Iron oxyhydroxides are represented by thermodynamically unstable amorphous $\delta-Fe^{3+}O(OH)$ feroxyhyte, with minor ferrihydrite $Fe_2O_3 \cdot 2FeOOH \cdot 2.5H_2O$. Feroxyhyte is formed with the influence of Fe^{2+} and ferrihydrite with Fe^{3+} , mainly due to oxydogenesis [84], both of which may form cements and coatings by rapid oxidation of other ferrous compounds. Ferrihydrite is considered as a predecessor of other more stable iron hydroxides [85]. Both minerals are major constituents of marine crusts and often coexist with clay minerals and goethite, and may transform in open-air conditions. The two minerals show yellowish-orange colors and in medium or slightly alkaline conditions form by oxidation of $Fe(OH)_2$ [86]. These show good absorptive properties and stability in oxidizing and alkaline conditions, forming during Eh (water melting) or pH increase (alkalization induced by water mixing) [87]. Domination of feroxyhyte suggests a leading role of variable redox conditions in the synthesis of hydroxides. Both mineral structures are stabilized by inorganic elements—silicon in ferrihydrite and manganese in feroxyhyte. Additionally, both minerals are associated with bacterial formation on lava flows, especially on the basalt- and gabbro-like hosted olivine and augite rocks [88]. Feroxyhyte and ferrihydrite may contain significant admixtures of Si, Al, Ba, Mg, P and Ca. Changes of Fe and Mn concentration in both phases may be an indicator of oscillatory changes of redox conditions, for example by oxygenated water inflows [89,90].

5.1.2. Phyllosilicates

Glaucosite is iron-rich hydrous silicate (Fe-rich mica) with a dioctahedral structure, within which considerable chemical variations can occur. The mineral can be found in widely differing sedimentary environments, in recent and fossil sediments. Additionally, celadonite, which is isomorphic with glaucosite, may occur in altered volcanic rocks. In the marine environment, both minerals form mixed-layered structures, often associated with clay minerals such as Fe-smectite and nontronite, especially in oxidizing conditions [91]. Glaucosite represents wide structural variability related to substitutions of Fe in tetrahedral and octahedral positions. Visible presence of phyllosilicate alteration (nontronite, chlorites and other clay minerals), connected with rapid Fe oxidation and Si presence, may induce transformation to ferroxhyte [92]. Nontronite in association with Fe-oxyhydroxides and glaucosite may be evidence of extensive oxidation processes, while celadonite and especially saponite rich mixtures are often associated with more redox conditions and alteration [93,94].

Layered silicates in the DHR samples are represented mainly by nontronite, Fe-smectite and Fe-rich glaucosite, with smaller amounts of Fe-bearing chlorites, celadonite and saponite (Figure 9a,b). All are depleted with Ni, Co, Cu, Ti, Mn and other metals. The K and Mg dominate over Na and Ca. Some of analyzed phyllosilicates have higher REE contents, varying from 23 to 653 ppm and Cr (20–1716 ppm). Chromium connected with phyllosilicates need to be considered as an indicator of intensive alteration processes. High content of Cl^- and $(\text{O}=\text{OH}^-)$ suggests percolative influence of salinated oceanic water and chlorine caption into the layered structures. Nontronite, celadonite and glaucosite are mainly intermixed, often with ferroxhyte and ferrihydrite. Mentioned mixtures dominate on substrate rock surfaces and in some fillings, veins and vesicles between colomorph generations and individual laminae. Nontronite was found also associated with zeolites and “palagonite” traces. Complete chemical results and empirical calculated formulas from the EPMA analysis are presented in Appendices A and B (Tables A1 and A2).

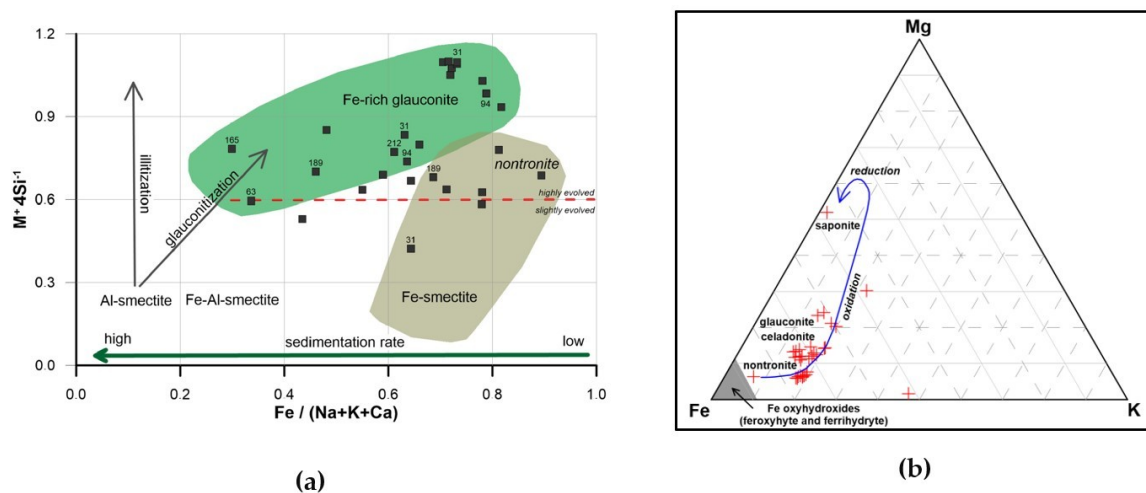


Figure 9. Variability of phyllosilicate minerals in crusts from the DHR: (a) phyllosilicate classification according to $Fe / (\Sigma Na, K, Ca)$ and $M^+ / 4Si$ ratios; compiled after [95,96]; (b) Ternary diagram classification of selected phyllosilicates basing on Fe-K-Mg ratios and oxidation-reduction potential [93].

Minor chlorite interlayers may be indicator of some lower temperature volcano-hydrothermal activity (>100 °C). Trace chlorites may form also due to initial water percolation within young cooling lavas [94].

5.1.3. Zeolites

Zeolites are hydrated aluminosilicates are often observed in marine environments and show exceptional ion-exchange and sorption properties. Zeolite structure is complex and composed of SiO_4

and AlO_4 tetrahedra. Substitution of Si by Al defines the negative charge of the zeolite crystalline framework, which is compensated by alkaline and earth alkaline metal cations. Exchangeable cations are mainly Na^+ , K^+ , Ca^{2+} , Mg^{2+} , Ba^{2+} and Sr^{2+} . Several metal substitutions, such as B, Fe, Cr, Ge and Ti may be present, especially in the Si lattice [97]. Zeolite chemistry is often associated with source rock composition [98] and occurs in the early stage of cavity crystallization mixtures with sequence of celadonite→glauconite→phillipsite-chabazite-heulandite. Presence of zeolites may be an indicator of higher environmental pH or near volcanic source. Phillipsite and chabazite members are typically associated with basalts and trachites [99]. Phillipsite may form during hydrothermal or diagenetic processes in the marine environment and is mainly a product of halmyrolisis of volcanoclastic material [100].

In the analyzed crusts, zeolites are mainly represented by low siliceous K-phillipsite, Na-chabazite and heulandite-clinoptilolite members (Figure 10). Investigated zeolites form coatings and small veins, mainly in the basalt-crust zone, mixed Mn-Fe oxyhydroxides and hydrated phosphates. The Si/Al ratio is in general low and varies from 2.20 to 3.15 (Table A1). The Ti/Al ratio in measured phillipsites is higher than in other zeolites and varies from 0.023 to 0.17 suggesting typical low hydrothermal basalt type rock genesis, compare [101]. Potassium content in the analyzed samples varies from 2.25% to 4.09%. Recognized phillipsites are represented mainly by K-phillipsite. Phillipsite exchanges irreversible Na for K, suggesting domination of authigenic formation and show some Fe and other metals impurities which may confirm these processes. Analyzed phillipsites show also some REE admixtures, mainly Y (165 to 653 ppm). Normally, marine phillipsites do not absorb REE and do not inherit the composition of the host rock [100]. Increased content of REE may be however connected with some diagenetic immobilization.

Chabazite is mainly hydrothermal but also a very rare diagenetic zeolite less common in the marine environment than phillipsite. Na-Chabazite is often associated with mafic rock cavities, being an indicator of diagenesis and low-grade metamorphism alteration, which forms assemblages with other zeolites and phyllosilicates [102]. The Si/Al ratio in analyzed Na-chabazite varies from 2.41 to 2.64, which is between hydrothermal and diagenetic formation [99]. Sodium dominates over calcium. The Ti/Al ratio is 0.0022. Chabazites have less impurities of Fe and Mn, less alkali than phillipsite and no traces of Ba and Sr. Sodium dominates over other alkali metals. Potassium content is intermediate (2.82–5.12%).

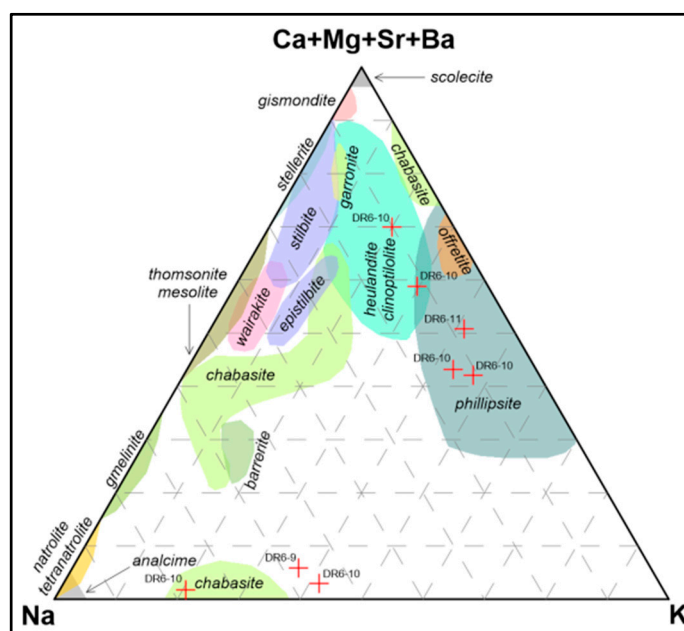


Figure 10. Ternary diagram classification of the DHR zeolites basing on Na, K and $\Sigma(\text{Ca}, \text{Mg}, \text{Sr}, \text{Ba})$ ratios. Compiled using References [103,104].

Heulandite-clinoptilolite group is also less common than phillipsite, but observed more often in pelagic sediments than in crusts and usually show diagenetic nature. The group is not stable in alkali environments, often substituted by phillipsite and other zeolites [99]. The analyzed clinoptilolite shows higher Ca content (6.95%) and Ba traces. The Si/Al ratio is 2.58. The clinoptilolite has some impurities of Fe and Mn, also admixtures of Ni, Co, Ti, Zn, S, P and Tl and is low in Na and Mg, with intermediate K content.

All geochemical data for DHR zeolites and their classification is presented in the Appendices A and B (Tables A1 and A2) and Figure 10.

5.1.4. Phosphates

The main mineral dominating the Co-rich ferromanganese crusts is amorphous apatite, especially hydroxyapatite or carbonatefluoroapatite (CPA), and its variations [9]. Hydroxyapatite has the general formula of $\text{Ca}_5(\text{PO}_4)_3(\text{F},\text{Cl},\text{OH})$ and is a structure that can incorporate a wide range of transition metals, REE and anions. Some common substitutions occurring in apatites are as follows [105,106]: Sr^{2+} , Mn^{2+} , Fe^{2+} , REE and Y^{3+} , Na^+ \leftrightarrow Ca^{2+} ; Si^{4+} , As^{5+} , S^{6+} and C^{4+} \leftrightarrow P^{5+} ; Cl^- and OH^- \leftrightarrow F^- ; 2Ca^{2+} \leftrightarrow $\text{Na}^+ + \text{REE}^{3+}$ and $\text{Ca}^{2+} + \text{P}^{5+}$ \leftrightarrow $\text{REE}^{3+} + \text{Si}^{4+}$. Phosphatization and precipitation of Fe-Mn oxyhydroxides may be indicators for change of hydrodynamic condition, oxygenated, fresh deep-water inflows or even upwelling currents [105,107].

In the samples from DHR, the Ca-hydroxyapatite was discovered to be a dominantly phosphate mineral, formed mainly as diagenetic-like coatings on the substrate basalts and between selected colomorphs. Minor occurrences were found in some detrital grains and biogenic ones (i.e., one sample with fish tooth). In general, apatites are pure one, without any detrital and authigenic impurities (Table A1). The Si/Al ratio is low and equal to 1.35, in general low in Cl^- (<0.11%) with traces of S (0.33–0.63 wt. %). Fluorine content varies from 0.28 to 3.56 wt. %. In general, the total REE content is high (mean 0.57 wt. %). The two EPMA sampling points with the highest F^- content (above 3 wt. %) show also the highest ΣREE contents, more than 1.8 wt. % of REE^{3+} and dominated by Y (0.64 to 0.98 wt. %). Normalized to PAAS chemical microprobe analyses of DHR hydroxylapatite, indicate negative Ce anomaly [43]. The REE pattern is typical for seamount phosphorites (Figure 11; compare [108]), as well as land-based phosphorites. Besides hydroxylapatite, some traces of Y (24–44 ppm) were also identified in stratified phyllosilicates (glaucinite, Fe-smectite and Fe-chlorite) and K-phillipsite (140–320 ppm).

The apatites from DHR exhibit phylloalteration and admixtures of K and Fe-rich minerals, such as glauconite and nontronite. Lower manganese and higher sulphur contents, comparing above, may be an indicators of oxygenation conditions [109]. The Mn/Fe ratio and total REY (Rare Earth Elements + Yttrium) sum confirms alteration, beside one sample of fish non-altered tooth, completely depleted with REE. The highest contents of ΣREY were observed in hydroxyapatites with P >14.2 wt. %, showing low chemical and mechanical impurities and increased volatiles content >3.0 wt. % (F, Cl and S), suggesting some hydrogenous acquisition of REE from external sources (positive correlation Cl with Na) and diagenetic immobilization.

The absence of visible XRD evidences of transformation of feroxyhyte/ferrihydrate into hematite or goethite, may suggest no weathering processes affecting crusts formation, even due to increasing maturity. The iron-rich minerals show higher substitution of Fe by Si, comparing vernadite and asbolane, and do not indicate visible traces of biogenic activity affecting formation processes (i.e., bacteria).

The samples described are ferromanganese marine deposits in type of Co-rich crusts, dominated by Co and Ni, and characterized by high Ti values. The ore is not sulfatized, partially highly phosphatized and alcalized (zeolitization). In general, the (bulk) samples, due to mean Ni content (<0.27%), need to be considered as a “poor ore” and according to mean Co amount (<0.29%) as a “medium-rich one”. Samples with asbolane domination (DR6-11) show higher contents of Li (>40 ppm) and Rb (>20 ppm), typical for asbolane-lithiophorite group. Vernadite dominated samples (DR6-9 and

DR6-10) exhibit greater amount of Mo (>300 ppm), V (>500 ppm), Th and U. The ore, in general, is depleted with Cr, Zn, Pb and Cu (mean Ni/Cu ratio is high as 3.76). There is no important content of Ag (<4 ppm) and Au, however some traces of Zr (mean >400 ppm), Ga, In and Os (more than few ppm) in the bulk ICP/MS and XRF analysis were observed and should be the aim of further investigation [30].

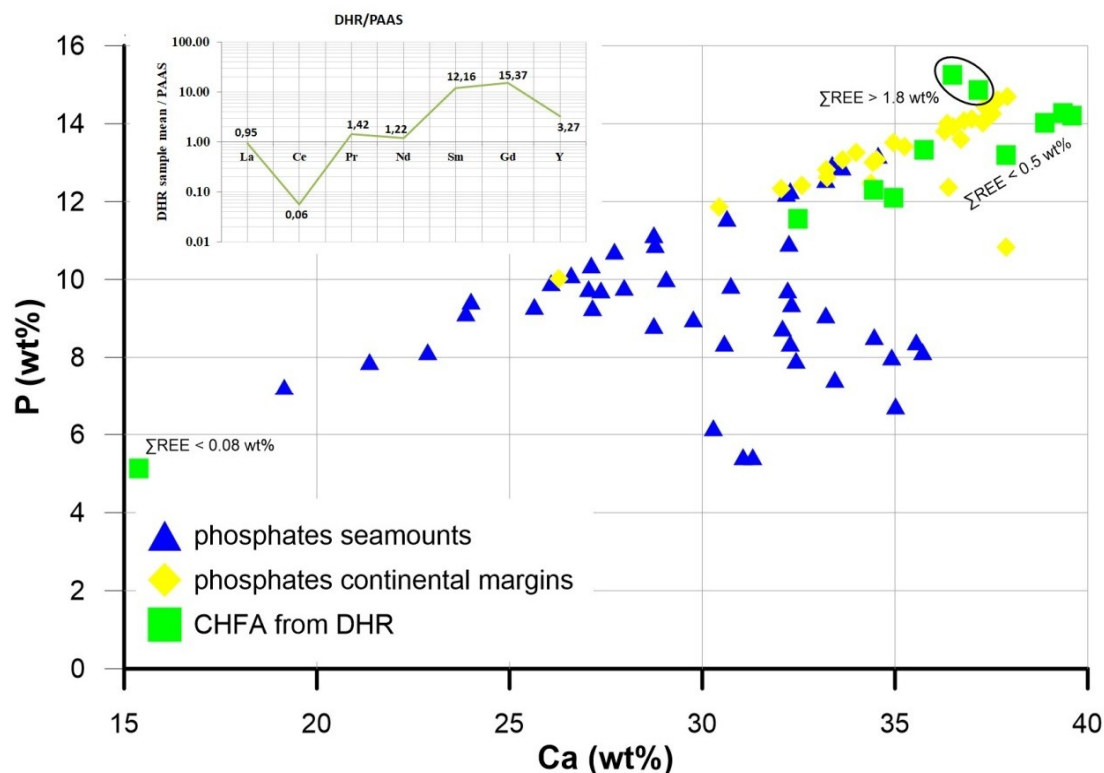


Figure 11. Scatter plot of phosphorus versus calcium in DHR Ca-hydroxyapatites. DHR crusts normalized to PAAS. Data for seamounts and continental margin phosphorite deposits from Reference [9]. The DHR data from EPMA.

6. Conclusions

Hydrogenous Co-rich ferromanganese crusts from the unique Dirck Hartog Ridge, located in the centre of Perth Abyssal Plain, E Indian Ocean were mineralogically analyzed and described.

Studied samples were composed mainly of Mn-vernadite, interlayered with smaller amount of Fe-vernadite, Ni-(Co) asbolanes and mixture of ferrosiderite–ferrihydrite. According to EPMA analysis and comparison of two different Mn/Fe ratios, the two subtypes of vernadite were identified: (I) Fe-(Mn) vernadite, defined by Mn/Fe ratio <1.0; (II) Mn-(Fe) vernadite, defined by Mn/Fe ratio >1.0. Some of identified vernadite laminae may be potentially 10 Å phyllosulfate in type busserite and some additional structural analysis shall be done. Compared to other Fe-Mn oxyhydroxides, vernadite laminae show typical hydrogenetic genesis, with the highest Pb, Ca, Ba, Sr, P and S contents. Vernadite also indicates the highest Co enrichment; however, the amount of other metals (Ni, Cu, Ti) is lower, compared to asbolane.

According to the mineralogical analysis, DHR crusts formation was dominated by three main processes: (I) basalt substrate rock weathering and alteration affected by phosphatization and glauconitization, (II) precipitation of Fe-Mn oxyhydroxides, mainly from the well oxidized ambient ocean waters, (III) sorption of metals by the Fe-Mn oxyhydroxides. The DHR crusts show low phosphorus content (<0.7%; mean 0.17%) suggesting rather the “young” generation.

Diagenetic asbolanes are represented mainly by Ni-asbolane, with extensive Mn⁴⁺ substitution. Asbolanes from the DHR indicate the highest contents of Ni, Cu, Zn, As and Tl, with some Na, K and Al

structural impurities, compared to vernadite and feroxyhyte-ferrihydrite. The metal content generally increases with the maturity of asbolane laminae. Asbolanes mainly impregnate crusts, whereas in the upper parts of crusts domination of vernadite is more distinctive.

The feroxyhyte–ferrihydrite mixtures show the highest contents of Si and Ti, being depleted in Mn and showing the lowest Ni, Cu and Co concentrations, compared to vernadite and asbolane. Phosphorus content is higher in feroxyhyte-ferrihydrite mixtures than in asbolanes.

Several analyzed phyllosilicates (Fe-smectite, nontronite, celadonite, glauconite, saponite and chlorites) show depletion with Ni, Cu and Co, especially within the intergrowths of Fe-Mn phases. However, glauconite, nontronite, celadonite and Fe-chlorites show some traces of Cr and Y.

Thermal analysis indicated large amounts of water incorporated into the structure of DHR crusts Fe-Mn oxyhydroxides, as well as high oxidation potential.

Formation of the Co-rich ferromanganese crusts from the DHR may result from the enhanced increase of Antarctic Bottom Water (AABW) current activity, beginning to occur in Indo-Pacific regions during early Miocene, which caused initial bedrock phosphatization, mainly due to increase of biogenic productivity and oxygen depletion. Global increase of sea level in the middle Miocene may have resulted oxygen enrichment and formation of analyzed Fe-Mn oxyhydroxides [110,111]. The proposed formation mechanism and growth model lie in good correspondence with some discovered diagenetic influences in asbolanes, which may indicate some periods of slower crusts growth in suboxic conditions, caused mainly by lesser impact of oxygene-rich water currents. Additionally, the presence of Ti-enriched feroxyhyte-ferrihydrite laminae, especially in deeper parts of the analyzed crust samples, may indicate initial basalt alteration and formation of Fe-rich oxyhydroxides due to rapid oxidation.

Author Contributions: Project idea: D.Z., Ł.M., R.A.K. and A.P.; Samples preparation: D.Z., Ł.M., G.A.K.-B., A.P. and R.J.W.; Microscope analysis and data interpretation: Ł.M., D.Z. and A.P.; XRD analysis and data interpretation, R.J.W. and Ł.M.; Thermal analysis and data interpretation: Ł.M.; EPMA analysis and data interpretation: G.A.K.-B., Ł.M., D.Z., A.P.; Writing: Ł.M., D.Z.; Funding acquisition: R.A.K., A.P., D.Z. and Ł.M.

Funding: The project was supported by statutory funds from Marine Geology Unit, University of Szczecin (grant No. 503-1100-230342). The electron microprobe analysis was possible thanks to funding obtained from AGH-UST statutory grant No. 11.11.140.161.

Acknowledgments: We would like to thank Joanne Whittaker, PhD, of the Institute for Marine and Antarctic Studies, University of Tasmania, Australia for providing the crusts samples, Teresa Radziejewska, PhD, provided advice and linguistic assistance. We are grateful to Kevin McCartney, PhD, of the University of Maine at Presque Isle, USA, for final linguistic correction of the manuscript. We also thank Iker Blasco, MSc, of the Instituto Geológico y Minero de España, Colegio Oficial de Geólogos, for graphical preparation of Figure 1, and Adam Gawęł, MSc, of the Department of Mineralogy, Petrography and Geochemistry, Faculty of Geology, Geophysics and Environmental Protection, AGH University of Science and Technology, provided XRD data of heated samples. We are also grateful to reviewers for valuable remarks which increased the quality of this paper.

Conflicts of Interest: The authors declare no conflicts of interest. The funders had no role in the design of the study; in the collection and interpretation of data; in the writing of the manuscript, and in the decision to publish the results.

Table A1. Cont.

Mineral Group	Vernadite		Asbolane		Feroxyhyte Ferrihydrite		Phyllosilicates					Phosphates		Zeolites		
	Fe-(Mn) 1	Mn-(Fe) 2	Ni-Cu- (Co) ³	Ni-Co- (Cu) ⁴	-	Ti-rich ⁵	Glauconite	Fe-smectite	Nontronite	Saponite	Celadonite	Fe-chlorite	Ca- hydroxyapatite	K- phillipsite	Na- chabazite	Na-heulandite Na-klinoptilote
Number of EPMA Analyses	n = 8	n = 56	n = 27	n = 9	n = 11	N = 8	N = 12	N = 6	N = 2	N = 8	N = 4	N = 2	N = 11	N = 4	N = 3	N = 1
Y ³⁺	-	-	-	-	-	-	0.001	-	-	-	-	-	0.012	0.001	-	-
La ³⁺	-	-	-	-	-	-	-	-	-	-	-	-	0.005	-	-	-
Ce ³⁺	-	-	-	-	-	-	-	-	-	-	-	-	0.001	-	-	-
Pr ³⁺	-	-	-	-	-	-	-	-	-	-	-	-	-	-	-	-
Nd ³⁺	-	-	-	-	-	-	-	-	-	-	-	-	0.004	-	-	-
Sm ³⁺	-	-	-	-	-	-	-	-	-	-	-	-	0.001	-	-	-
Gd ³⁺	-	-	-	-	-	-	-	-	-	-	-	-	0.001	-	-	-
Tb ³⁺	-	-	-	-	-	-	-	-	-	-	-	-	-	-	-	-
Dy ³⁺	-	-	-	-	-	-	-	-	-	-	-	-	-	-	-	-
Ho ³⁺	-	-	-	-	-	-	-	-	-	-	-	-	-	-	-	-
Er ³⁺	-	-	-	-	-	-	-	-	-	-	-	-	-	-	-	-
Tm ³⁺	-	-	-	-	-	-	-	-	-	-	-	-	-	-	-	-
Yb ³⁺	-	-	-	-	-	-	-	-	-	-	-	-	-	-	-	-
Lu ³⁺	-	-	-	-	-	-	-	-	-	-	-	-	-	-	-	-
Eu ³⁺	-	-	-	-	-	-	-	-	-	-	-	-	-	-	-	-
Hf ⁴⁺	-	-	-	-	-	-	-	-	-	-	-	-	-	-	-	-
ΣREE ³⁺	-	-	-	-	-	-	0.001	-	-	-	-	-	0.024	0.001	-	-
U ⁴⁺	-	-	-	-	-	-	-	-	-	-	-	-	-	-	-	-
Th ⁴⁺	-	-	-	-	-	-	-	-	-	-	-	-	-	-	-	-
Σ _{ion}	6	6	3	3	3	3	7	6.5	6.5	7	7	6	9	10	7	10
No oxyg. at.	8	8	4	4	4	4	12	19.5	21.5	20.5	12	12	13	22	18	24

¹ Iron dominated; Mn/Fe < 1.0. ² Manganese dominated; Mn/Fe > 1.0. ³ Copper dominated; Co/Cu < 1.0. ⁴ Cobalt dominated; Co/Cu > 1.0. ⁵ Titanium rich; Ti > 1.0 [wt. %]. * Fe³⁺ calculated from the stoichiometry. ** Mn⁴⁺ calculated for the structural formula of vernadite.

Appendix B

Table A2. The mean calculated empirical formulas of DHR Co-rich crusts minerals (basing on the EPMA data).

Basalt Substrate	
Feldspars	
Bytownite	
$(\text{Ca}_{0.463} \text{K}_{0.321} \text{Na}_{0.188} \text{Mg}_{0.012} \text{Ti}_{0.001}) \Sigma = 0.985$ $(\text{Si}_{2.552} \text{Al}_{1.437} \text{Fe}_{0.026} \text{Cr}_{0.001}) \Sigma = 4.016$ O_8	
Labradorite	
$(\text{Ca}_{0.490} \text{Na}_{0.470} \text{K}_{0.021} \text{Mg}_{0.007} \text{Ti}_{0.003} \text{Y}_{0.001}) \Sigma = 0.992$ $(\text{Si}_{2.500} \text{Al}_{1.462} \text{Fe}_{0.046}) \Sigma = 4.008$ O_8	
Albite	
$[\text{Cl}^-_{0.002}] (\text{Na}_{0.754} \text{Ca}_{0.021} \text{K}_{0.021} \text{Mn}_{0.019} \text{Ti}_{0.003} \text{Mg}_{0.003}) \Sigma = 0.800$ $(\text{Si}_{3.092} \text{Al}_{1.061} \text{Fe}_{0.027}) \Sigma = 4.18$ O_8	
Orthoclase (or sanidine)	
$[\text{Cl}^-_{0.001}] (\text{K}_{0.943} \text{Na}_{0.004} \text{Ca}_{0.001} \text{Ti}_{0.001} \text{Mn}_{0.002}) \Sigma = 0.951$ $(\text{Si}_{3.046} \text{Al}_{0.996} \text{Fe}_{0.004} \text{Cr}_{0.004}) \Sigma = 4.05$ O_8	
Pyroxenes	
Diopside	
$[\text{Cl}^-_{0.001}] (\text{Ca}_{0.766} \text{Fe}^{2+}_{0.188} \text{Mg}_{0.030} \text{Na}_{0.016}) \Sigma = 1.000$ $(\text{Mg}_{0.895} \text{Al}_{0.055} \text{Ti}_{0.019} \text{Cr}_{0.019} \text{Mn}_{0.011}) \Sigma = 1.000$ $(\text{Si}_{1.927} \text{Al}_{0.073}) \Sigma = 2.000$ O_6	
Augite	
$[\text{Cl}^-_{0.003}] (\text{Ca}_{0.356} \text{Na}_{0.301} \text{Fe}^{2+}_{0.221} \text{K}_{0.068} \text{Mg}_{0.027} \text{Mn}_{0.015}) \Sigma = 0.988$ $(\text{Al}_{0.469} \text{Mg}_{0.416} \text{Fe}^{2+}_{0.103} \text{Ti}_{0.012}) \Sigma = 1.000$ $(\text{Si}_{1.949} \text{Al}_{0.051}) \Sigma = 2.000$ O_6	
Ferrosilite	
$[\text{Cl}^-_{0.008}] (\text{Mg}_{0.247} \text{Fe}^{2+}_{0.205} \text{K}_{0.183} \text{Ti}_{0.079} \text{Na}_{0.039} \text{Ca}_{0.021} \text{Mn}_{0.008}) \Sigma = 0.782$ $(\text{Al}_{0.721} \text{Fe}^{2+}_{0.279}) \Sigma = 1.000$ $(\text{Si}_{2.210}) \Sigma = 2.210$ O_6	
Other	
Pseudobrookite	
$(\text{Fe}^{3+}_{1.212} \text{Fe}^{2+}_{0.687} \text{Al}_{0.043} \text{Mg}_{0.040} \text{Mn}_{0.013} \text{Ba}_{0.006} \text{Zn}_{0.005} \text{Si}_{0.003} \text{Na}_{0.003} \text{Ca}_{0.003} \text{Co}_{0.003} \text{K}_{0.002} \text{Ni}_{0.002} \text{Cu}_{0.001} \text{Ti}_{0.001}) \Sigma = 2.067$ $(\text{Ti}_{0.667} \text{Fe}^{3+}_{0.333}) \Sigma = 1.000$ O_5	
Mg-chromite	
$(\text{Mg}_{0.538} \text{Fe}^{2+}_{0.464} \text{Ti}_{0.017} \text{Mn}_{0.007} \text{Ca}_{0.005} \text{Zn}_{0.002} \text{Ni}_{0.002} \text{Co}_{0.001}) \Sigma = 1.036$ $(\text{Cr}_{1.012} \text{Al}_{0.770} \text{Fe}^{3+}_{0.175} \text{V}_{0.004} \text{Si}_{0.002}) \Sigma = 1.963$ O_4	
Zircon	
$(\text{Zr}_{0.941} \text{REE}^{3+}_{0.054} \text{Fe}^{3+}_{0.019} \text{Hf}_{0.008} \text{Ti}_{0.004}) \Sigma = 1.026$ $\text{Si}_{0.975}$ O_4	
Basalt Substrate—Crust Transition Zone	
Phosphates	
Ca-hydroxyfluorapatite (CFA)	
$(\text{Ca}_{4.656} \text{Na}_{0.125} \text{Fe}_{0.081} \text{Mg}_{0.052} \text{K}_{0.026} \text{REE}^{3+}_{0.024} \text{Ti}_{0.020} \text{Cu}_{0.008} \text{Mn}_{0.004} \text{Sr}_{0.002} \text{Zn}_{0.001}) \Sigma = 4.999$ $[(\text{PO}_4)_{2.221} (\text{CO}_3)_{0.093} (\text{SiO}_2)_{0.235} \text{Al}_2\text{O}_3)_{0.127} (\text{SO}_3)_{0.139}] \Sigma = 2.815$ $[(\text{OH})_{0.949} \text{F}_{0.326} \text{Cl}_{0.004}] \Sigma = 1.279$	
Zeolites	
Na-chabazite	
$[\text{OH}^-_{1.235}] \Sigma = 1.235$ $(\text{Na}_{1.130} \text{K}_{0.333} \text{Ca}_{0.030} \text{Fe}^{2+}_{0.020} \text{Mg}_{0.012} \text{Mn}_{0.004} \text{Ti}_{0.003} \text{Cr}_{0.001}) \Sigma = 1.533$ $(\text{Al}_{1.225} \text{Si}_{3.007}) \Sigma = 4.232$ $\text{O}_{11.5} \times 6.5 \text{H}_2\text{O}$	
Ca-heulandite (or Ca-klinoptilolite)	
$[\text{Cl}^-_{0.003} \text{OH}^-_{1.445}] \Sigma = 1.448$ $(\text{Ca}_{0.876} \text{K}_{0.271} \text{Na}_{0.231} \text{Mg}_{0.079} \text{Ba}_{0.001}) \Sigma = 1.458$ $(\text{Si}_{4.785} \text{Al}_{1.932} \text{P}_{0.285} \text{Fe}_{0.053} \text{S}_{0.023} \text{Ti}_{0.011} \text{Zn}_{0.002} \text{Co}_{0.001} \text{Ti}_{0.001}) \Sigma = 7.093$ $\text{O}_{17.5} \times 4.5 \text{H}_2\text{O}$	
K-phillipsite	
$[\text{Cl}^-_{0.012} \text{OH}^-_{1.372}] \Sigma = 1.384$ $(\text{Fe}_{0.562} \text{Mg}_{0.404} \text{K}_{0.368} \text{Ca}_{0.196} \text{Na}_{0.176} \text{Mn}_{0.061} \text{Ni}_{0.006} \text{Cu}_{0.004} \text{S}_{0.003} \text{As}_{0.002} \text{Zn}_{0.001} \text{Cr}_{0.001} \text{P}_{0.001} \text{Y}_{0.001}) \Sigma = 1.786$ $(\text{Si}_{4.713} \text{Al}_{1.831}) \Sigma = 6.544$ $\text{O}_{16} \times 6.0 \text{H}_2\text{O}$	

Table A2. Cont.

Phyllosilicates	
	Glauconite $[Cl^-_{0.011}] (K_{0.467} Mg_{0.367} Ca_{0.042} Na_{0.111}) \Sigma = 0.987 (Fe^{3+}_{0.318} Mg_{0.116} Fe^{2+}_{0.981} Al_{0.563} Ti_{0.013} Mn_{0.005} S_{0.002} Cr_{0.001} Y_{0.001})$ $\Sigma = 2.000 (Si_{3.803} Al_{0.197}) \Sigma = 4.000 O_{10} (OH)_2$
	Nontronite $[Cl^-_{0.009}] Ca_{0.026} Fe^{2+}_{0.534} (Fe^{3+}_{0.909} Mg_{0.570} K_{0.398} Al_{0.262} Na_{0.100} Cr_{0.006} Mn_{0.001}) \Sigma = 2.246 (Si_{3.685} Al_{0.262}) \Sigma = 3.947 O_{10} (OH)_2$ $\times 9.5 H_2O$
	Fe-smectite $[Cl^-_{0.013}] (Ca_{0.046} Na_{0.122}) \Sigma = 0.168 (Al_{0.690} Mg_{0.440} Fe_{0.834} Ti_{0.049} Mn_{0.005} Cr_{0.003}) \Sigma = 2.021 (Si_{3.572} Al_{0.428}) \Sigma = 4.000 O_{10} (OH)_2$ $\times 7.5 H_2O$
	Saponite $[Cl^-_{0.007}] (Ca_{0.025} Na_{0.083} K_{0.488}) \Sigma = 0.596 (Mg_{0.447} Fe^{2+}_{0.566} Fe^{3+}_{1.105} Al_{0.257} Ti_{0.009} Mn_{0.007} Zn_{0.001} S_{0.004}) \Sigma = 2.396 (Si_{3.763} Al_{0.237}) \Sigma = 4.000 O_{10} (OH)_2 \times 8.5 H_2O$
	Celadonite $[Cl^-_{0.011}] (Mg_{0.475} K_{0.384} Na_{0.109} Ca_{0.020}) \Sigma = 0.988 (Mg_{0.062} Fe^{3+}_{0.491} Fe^{2+}_{0.427} Ti_{0.014} Cr_{0.003} Mn_{0.001} S_{0.001} As_{0.001}) \Sigma = 1.000$ $(Fe^{3+}_{0.600} Al_{0.400}) \Sigma = 1.000$ $(Si_{3.946} Al_{0.054}) \Sigma = 4.000 O_{10} (OH)_2$
	Fe-chlorite $[Cl^-_{0.016}] (Fe^{2+}_{1.549} Mg_{0.410} Na_{0.097} Mn_{0.048} Ca_{0.019} K_{0.003}) \Sigma = 2.126 (Fe^{3+}_{0.877} Al_{0.569} Si_{0.384} Ti_{0.027}) \Sigma = 1.857 Si_{2.000} O_{9.800}$ $(OH)_{3.200}$
Fe-Mn Crusts Zone	
Fe-Mn oxyhydroxides	
	Fe-(Mn) Vernadite $[Cl^-] \Sigma = 0.092 (Mn^{4+}_{1.715} Si_{0.791} Ti_{0.232}) \Sigma = 2.738 (Na_{0.127} K_{0.028}) \Sigma = 0.155 (Ca_{0.214} Mg_{0.156} Sr_{0.079} Co_{0.026} Ni_{0.018} Ba_{0.015} Cu_{0.009}$ $Zn_{0.009} Pb_{0.006}) \Sigma = 0.532$ $(Fe^{3+}_{2.416} Al_{0.230} As_{0.001}) \Sigma = 2.647 (P_{0.063} S^{6+}_{0.050}) \Sigma = 0.113 \times 1.72 H_2O$
	Mn-(Fe) Vernadite $[Cl^-] \Sigma = 0.097 (Mn^{4+}_{2.662} Si_{0.376} Ti_{0.114}) \Sigma = 3.052 (Na_{0.157} K_{0.033}) \Sigma = 0.190 (Ca_{0.325} Mg_{0.197} Sr_{0.042} Co_{0.069} Ni_{0.043} Ba_{0.008} Cu_{0.012}$ $Zn_{0.007} Pb_{0.003}) \Sigma = 0.706$ $(Fe^{3+}_{1.586} Al_{0.133} As_{0.001}) \Sigma = 1.720 (P_{0.037} S^{6+}_{0.079}) \Sigma = 0.116 \times 2.00 H_2O$
	Ni-Cu-(Co) Asbolane $[Cl^-_{0.012} S^{6+}_{0.009} P_{0.005}] \Sigma = 0.026 (Mg_{0.410} Ni_{0.127} Ca_{0.067} Cu_{0.032} Zn_{0.013} Sr_{0.008} Co_{0.006} Ba_{0.003}) \Sigma = 0.666 (Mn^{2+}_{1.857} Al_{0.183}$ $Fe^{3+}_{0.067} Si_{0.061} Ti_{0.012} As_{0.001}) \Sigma = 2.181 (Na_{0.097} K_{0.050}) \Sigma = 0.147 \times 0.98 H_2O$
	Ni-Co-(Cu) Asbolane $[Cl^-_{0.012} S^{6+}_{0.008} P_{0.006}] \Sigma = 0.026 (Mg_{0.308} Ni_{0.170} Ca_{0.095} Co_{0.029} Cu_{0.012} Sr_{0.008} Zn_{0.007} Ba_{0.003}) \Sigma = 0.632 (Mn^{2+}_{1.779} Al_{0.126}$ $Fe^{3+}_{0.095} Si_{0.043} Ti_{0.020}) \Sigma = 2.063$ $(Na_{0.151} K_{0.038}) \Sigma = 0.189 \times 1.09 H_2O$
	* Feroxyhyte Ferrihydrite $nFe_2O_3 \times nH_2O$ $[Cl^-_{0.006}] \Sigma = 0.006 (Fe^{3+}_{2.349} Si_{0.534} Al_{0.088} Mg_{0.082} P_{0.017} Na_{0.012} K_{0.011} Ca_{0.011} Cu_{0.005} Co_{0.004} Ti_{0.004} Mn_{0.003} Zn_{0.003} S_{0.003}$ $Ni_{0.002}) \Sigma = 3.128 \times 0.87 H_2O$
	* (Ti)-Feroxyhyte (Ti)-Ferrihydrite $nFe_2O_3 \times nH_2O$ $[Cl^-_{0.027}] \Sigma = 0.027 (Fe^{3+}_{1.928} Si^{4+}_{0.514} Ti_{0.267} Al_{0.168} Mg_{0.098} Ca_{0.053} P_{0.043} Na_{0.022} Sr_{0.018} K_{0.014} S_{0.009} Cu_{0.008} Zn_{0.005} Co_{0.004}$ $Ba_{0.004} Mn_{0.003} Ni_{0.002} Pb_{0.001} As_{0.001}) \Sigma = 3.162 \times 0.81 H_2O$
* Empirical formulas of feroxyhyte and ferrihydrite, due to lack of structural data, were calculated using generalized $nFe_2O_3 \times nH_2O$.	

References

- Hodkinson, R.A.; Cronan, D.S. Regional and depth variability in the composition of cobalt-rich ferromanganese crusts from the SOPAC area and adjacent parts of the central equatorial Pacific. *Mar. Geol.* **1991**, *98*, 437–447. [[CrossRef](#)]
- Hein, J.R. Cobalt-Rich Ferromanganese Crusts: Global Distribution, Composition, Origin and research Activities. In *Polymetallic Massive Sulphides and Cobalt-Rich Ferromanganese Crusts: Status and Prospects*; ISA Technical Study 2; International Seabed Authority: Kingston, Jamaica, 2002; pp. 36–89.
- Hein, J.R.; Koschinsky, A.; Bau, M.; Manheim, F.; Kang, J.-K.; Roberts, L. Cobalt-Rich Ferromanganese Crusts in the Pacific. In *Handbook of Marine Mineral Deposits*; Cronan, D., Ed.; CRC Press: London, UK, 2000; pp. 239–272.

4. Hein, J.R.; Conrad, T.A.; Dunham, R.E. Seamount Characteristics and Mine-Site Model Applied to Exploration- and Mining-Lease-Block Selection for Cobalt-Rich Ferromanganese Crust. *Mar. Georesources Geotechnol.* **2009**, *27*, 160–176. [[CrossRef](#)]
5. Cui, Y.; Liu, J.; Ren, X.; Shi, X. Geochemistry of rare earth elements in cobalt-rich crusts from the Mid-Pacific M seamount. *J. Rare Earths* **2009**, *27*, 169–176.
6. Zawadzki, D. The state of knowledge and possibilities to extract strategic raw materials from the ocean poly metallic deposits [Stan rozpoznania i możliwości pozyskiwania metali strategicznych z polimetalicznych kopalni oceanicznych]. *Prz. Geol.* **2013**, *61*, 45–53.
7. Hein, J.R.; Koschinsky, A. Deep-Ocean Ferromanganese Crusts and Nodules. In *Treatise on Geochemistry*, 2nd ed.; Holland, H.D., Turekian, K.K., Eds.; Elsevier: Amsterdam, The Netherlands, 2014; Volume 13, pp. 273–291.
8. Szamalek, K. The state of knowledge concerning on oceanic mineral resources [Stan rozpoznania oceanicznych zasobów mineralnych]. *Prz. Geol.* **2018**, *66*, 189–194.
9. Hein, J.R.; Conrad, T.; Mizell, K.; Banakar, V.K.; Frey, F.A.; Sager, W.W. Controls on ferromanganese crust composition and reconnaissance resource potential, Ninetyeast Ridge, Indian Ocean. *Deep-Sea Res. I* **2016**, *110*, 1–19. [[CrossRef](#)]
10. Konstantinova, N.; Cherkashov, G.; Hein, J.R.; Mirão, J.; Dias, P.; Madureira, P.; Kuznetsov, V.; Maksimov, F. Composition and characteristics of the ferromanganese crusts from the western Arctic Ocean. *Ore Geol. Rev.* **2017**, *87*, 88–99. [[CrossRef](#)]
11. Conrad, T.; Hein, J.R.; Paytan, A.; Clague, D.A. Formation of Fe-Mn crusts within a continental margin environment. *Ore Geol. Rev.* **2017**, *87*, 25–40. [[CrossRef](#)]
12. Marino, E.; González, F.J.; Lunar, R.; Reyes, J.; Medialdea, T.; Castillo-Carrión, M.; Bellido, E.; Somoza, L. High-Resolution Analysis of Critical Minerals and Elements in Fe–Mn Crusts from the Canary Island Seamount Province (Atlantic Ocean). *Minerals* **2018**, *8*, 285. [[CrossRef](#)]
13. Hein, J.R. Cobalt-rich ferromanganese crusts: Global distribution, composition, origin and research activities. In *Minerals Other than Polymetallic Nodules of the International Seabed Area*; International Seabed Authority: Kingston, Jamaica, 2004; Chapter 5; pp. 188–256.
14. Hein, J.R.; Koschinsky, A. Deep-ocean ferromanganese crusts and nodules. In *The Treatise on Geochemistry*; Scott, S., Ed.; Elsevier: Amsterdam, The Netherlands, 2013; Volume 12, pp. 273–290. [[CrossRef](#)]
15. Hein, J.R.; Koschinsky, A.; Halbach, P.; Manheim, F.T.; Bau, M.; Kang, J.K.; Lubick, N. Iron and manganese oxide mineralization in the Pacific. In *Manganese Mineralization: Geochemistry and Mineralogy of Terrestrial and Marine Deposits*; Special Publications; Nicholson, K., Hein, J.R., Bühn, B., Dasgupta, S., Eds.; Geological Society: London, UK, 1997; Volume 119, pp. 123–138.
16. Hein, J.R.; Conrad, T.; Staudigel, H. Seamount mineral deposits. A source of rare metals for high-technology industries. *Oceanography* **2010**, *23*, 184–189. [[CrossRef](#)]
17. Petersen, S.; Krättschell, A.; Augustin, N.; Jamieson, J.; Hein, J.; Hannington, M.D. News from the seabed—Geological characteristics and resource potential of deep sea mineral resources. *Mar. Policy* **2016**, *70*, 175–187. [[CrossRef](#)]
18. Zhong, Y.; Chen, Z.; González, F.J.; Hein, J.R.; Zheng, X.; Li, G.; Luo, Y.; Mo, A.; Tian, Y.; Wang, S. Composition and genesis of ferromanganese deposits from the northern South China Sea. *J. Asian Earth Sci.* **2017**, *138*, 110–128. [[CrossRef](#)]
19. Fitzgerald, C.E.; Gillis, K.M. Hydrothermal manganese oxide deposits from Baby Bare seamount in the Northeast Pacific Ocean. *Mar. Geol.* **2006**, *225*, 145–156. [[CrossRef](#)]
20. Baturin, G.N.; Dobretsova, I.G.; Dubinchuk, V.T. Hydrothermal manganese mineralization in the Peterburgskoye ore field (North Atlantic). *Oceanology* **2014**, *54*, 222–230. [[CrossRef](#)]
21. González, F.J.; Somoza, L.; Hein, J.R.; Medialdea, T.; León, R.; Urgorri, V.; Reyes, J.; Martín-Rubí, J.A. Phosphorites, Co-rich Mn nodules, and Fe-Mn crusts from Galicia Bank, NE Atlantic: Reflections of Cenozoic tectonics and paleoceanography. *Geochem. Geophys. Geosyst.* **2016**, *17*, 346–374. [[CrossRef](#)]
22. Hein, J.R.; Mizell, K.; Koschinsky, A.; Conrad, T.A. Deep-ocean mineral deposits as a source of critical metals for high- and green-technology applications: Comparison with land-based resources. *Ore Geol. Rev.* **2013**, *51*, 1–14. [[CrossRef](#)]

23. Asavin, A.M.; Kubrakova, I.V.; Mel'nikov, M.E.; Tyutyunnik, O.A.; Chesalova, E.I. Geochemical Zoning in Ferromanganese Crusts of Ita-MaiTai Guyot. *Geochem. Int.* **2010**, *48*, 423–445. [[CrossRef](#)]
24. Dubinin, A.V.; Uspenskaya, T.Y. Geochemistry and specific features of manganese ore formation in sediments of oceanic bioproductive zones. *Lithol. Miner. Resour.* **2006**, *41*, 1–14. [[CrossRef](#)]
25. Andreev, S.I. (Ed.) *Cobalt Rich Ores in the World Ocean*; VNII Okeangeologiya: St. Petersburg, Russia, 2002. (In Russian)
26. Asavin, A.M.; Anikeeva, L.I.; Kazakova, V.A.; Andreev, S.I.; Sapozhnikov, D.A.; Roshchina, I.A.; Kogarko, L.N. Trace element and PGE distribution in layered ferromanganese crusts. *Geochem. Int.* **2008**, *46*, 1179–1205. [[CrossRef](#)]
27. Novikov, G.V.; Yashina, S.V.; Melnikov, M.E.; Vikentev, I.V.; Bogdanova, O.Y. Nature of Co-Bearing Ferromanganese Crusts of the Magellan Seamounts (Pacific Ocean): Communication 2. Ion Exchange Properties of Ore Minerals. *Lithol. Miner. Resour.* **2014**, *49*, 138–164. [[CrossRef](#)]
28. ISA Central Data Repository. Available online: <https://www.isa.org.jm> (accessed on 1 September 2018).
29. Hein, J.R. Cobalt-Rich Ferromanganese Crusts: Global Distribution, Composition, Origin and Research Activities. In *Polymetallic Massive Sulphides and Cobalt-Rich Ferromanganese Crusts: Status and Prospects*; International Seabed Authority: Kingston, Jamaica, 2004; pp. 188–256.
30. Zawadzki, D.; Maciag, Ł.; Kotliński, R.A.; Kozub-Budzyń, G.A.; Piestrzyński, A.; Wróbel, A. Geochemistry of cobalt-rich ferromanganese crusts from the Perth Abyssal Plain (E Indian Ocean). *Ore Geol. Rev.* **2018**, *101*, 520–531. [[CrossRef](#)]
31. Watson, S.J.; Whittaker, J.M.; Halpin, J.A.; Williams, S.E.; Milan, L.A.; Daczko, N.R.; Wyman, D.A. Tectonic drivers and the influence of the Kerguelen plume on seafloor spreading during formation of the Early Indian Ocean. *Gondwana Res.* **2016**, *35*, 97–114. [[CrossRef](#)]
32. Whittaker, J.M.; Halpin, J.A.; Williams, S.E.; Hall, L.S.; Gardner, R.; Kobler, M.E.; Daczko, N.R.; Müller, R.D. Tectonic Evolution and Continental Fragmentation of the Southern West Australian Margin. In Proceedings of the West Australian Basins Symposium, Perth, Australia, 18–21 August 2013.
33. Gibbons, A.; Barckhausen, U.; Van Den Bogaard, P.; Hoernle, K.; Werner, R.; Whittaker, J.M.; Müller, R.D. Constraining the Jurassic extent of Greater India: Tectonic evolution of the Australian margin. *Geochem. Geophys. Geosyst.* **2012**, *13*. [[CrossRef](#)]
34. Cresswell, G.R.; Peterson, J.L. The Leeuwin Current south of Western Australia. *Aust. J. Mar. Freshw. Res.* **1993**, *44*, 285–303. [[CrossRef](#)]
35. Richardson, L.; Mathews, E.; Heap, A. *Geomorphology and Sedimentology of the South Western Planning Area of Australia. Review and Synthesis of Relevant Literature in Support of Regional Marine Planning*; Geoscience Australia: Canberra, Australia, 2005.
36. IHO-IOC. GEBCO Gazetteer of Undersea Feature Names. 2006 version. Available online: https://www.gebco.net/data_and_products/undersea_feature_names/ (accessed on 29 January 2019).
37. Williams, S.E. The Perth Abyssal Plain: Understanding Eastern Gondwana Break-Up, RV Southern Surveyor Voyage SS2011_v06 Scientific Highlights. CSIRO, 2011. Available online: <http://www.marine.csiro.au/nationalfacility/voyagedocs/2011/index.htm> (accessed on 4 September 2018).
38. Williams, S.E.; Whittaker, J.M.; Granot, R.; Müller, D.R. Early India-Australia spreading history revealed by newly detected Mesozoic magnetic anomalies in the Perth Abyssal Plain. *J. Geophys. Res. Solid Earth* **2013**, *118*, 3275–3284. [[CrossRef](#)]
39. Williams, S.E.; Whittaker, J.M.; Müller, D.R. Newly-recognised Continental Fragments Rifted from the West Australian Margin. In Proceedings of the West Australian Basins Symposium, Perth, Australia, 18–21 August 2013.
40. Grazulis, S.; Chateigner, D.; Downs, R.T.; Yokochi, A.T.; Quiros, M.; Lutterotti, L.; Manakova, E.; Butkus, J.; Moeck, P.; Le Bail, A. Crystallography Open Database—An open-access collection of crystal structures. *J. Appl. Cryst.* **2009**, *42*, 726–729. [[CrossRef](#)]
41. Paulik, F.; Paulik, J.; Erdey, L. Derivatography—A complex Method in Thermal Analysis. *Talanta* **1966**, *13*, 1405–1430. [[CrossRef](#)]
42. Musiał, W. Derywat—Data Acquisition System for Thermoanalysis. 2010. Available online: <http://www.w-musial.home.pl> (accessed on 1 May 2015).

43. Taylor, S.R.; McLennan, S.M. *The Continental Crust: Its Composition and Evolution*; Blackwell Scientific Publications: Carlton, Australia, 1985; pp. 1–312.
44. Steinfink, H. The crystal structure of the zeolite phillipsite. Locality: Pelagic sediments of the Pacific Ocean. *Acta Crystallogr.* **1962**, *15*, 644–651. [[CrossRef](#)]
45. Gualtieri, A.F. Study of NH_4^+ in the zeolite phillipsite by combined synchrotron powder diffraction and IR spectroscopy. *Acta Crystallogr.* **2000**, *56*, 584–593. [[CrossRef](#)]
46. Borisov, S.V.; Klevtsova, R.F. Crystal Structure of Rare-Earth-Strontium-Apatite. *Zhurnal Strukturnoi Khimii* **1963**, *4*, 629–631.
47. Fleet, M.E.; Liu, X. Accommodation of the carbonate ion in fluorapatite synthesized at high pressure. *Am. Mineral.* **2008**, *93*, 1460–1469. [[CrossRef](#)]
48. Wenk, H.R.; Joswig, W.; Tagai, T.; Korekawa, M.; Smith, B.K. The average structure of An_{62-66} labradorite. *Am. Mineral.* **1980**, *65*, 81–95.
49. FitzGerald, J.D.; Parise, J.B.; Mackinnon, I.D.R. Average structure of an An_{48} plagioclase from the Hogarth Ranges. *Am. Mineral.* **1986**, *71*, 1399–1408.
50. Raudsepp, M.; Hawthorne, F.C.; Turnock, A.C. Crystal chemistry of synthetic pyroxenes on the join $\text{CaNiSi}_2\text{O}_6$ – $\text{CaMgSi}_2\text{O}_6$ (diopside): A Rietveld refinement study. *Am. Mineral.* **1990**, *75*, 1274–1281.
51. Gualtieri, A.F. Accuracy of XRPD QPA using the combined Rietveld-RIR method. *J. Appl. Crystallogr.* **2000**, *33*, 267–278. [[CrossRef](#)]
52. Drits, V.A.; Zviagina, B.B.; McCarty, D.K.; Salyn, A.L. Factors responsible for crystal-chemical variations in the solid solutions from illite to aluminoceladonite and from glauconite to celadonite. *Am. Mineral.* **2010**, *95*, 348–361. [[CrossRef](#)]
53. Ewart, A. The Mineralogy and Petrology of Tertiary-Recent Orogenic Volcanic Rocks: With a Special Reference to the Andesitic-Basaltic Compositional Range. In *Andesites: Orogenic Andesites and Related Rocks*; Thorpe, R.S., Ed.; Wiley: Chichester, UK, 1982; pp. 25–95.
54. Winchester, J.A.; Floyd, P.A. Geochemical discrimination of different magma series and their differentiation products using immobile elements. *Chem. Geol.* **1977**, *20*, 325–343. [[CrossRef](#)]
55. Frost, B.R.; Frost, C.D. A geochemical classification for feldspathic igneous rocks. *J. Petrol.* **2008**, *49*, 1955–1969. [[CrossRef](#)]
56. Pearce, J.A.; Gale, G.H. *Identification of Ore-Deposition Environment from Trace-Element Geochemistry of Associated Igneous Host Rocks*; Special Publications; Geological Society: London, UK, 1977; Volume 7, pp. 14–24.
57. Pearce, J.A. Role of the Sub-Continental Lithosphere in Magma Genesis at Active Continental Margins. In *Continental Basalts and Mantle Xenoliths*; Hawkesworth, C.J., Norry, M.J., Eds.; Shiva: Nantwich, UK, 1983; pp. 230–249.
58. Mullen, E.D. $\text{MnO}/\text{TiO}_2/\text{P}_2\text{O}_5$: A minor element discriminant for basaltic rocks of oceanic environments and its implications for petrogenesis. *Earth Planet. Sci. Lett.* **1983**, *62*, 53–62. [[CrossRef](#)]
59. Földvári, M. Handbook of the thermogravimetric system of minerals and its use in geological practice. In *Occasional Papers of the Geological Institute of Hungary*; Geological Institute of Hungary: Budapest, Hungary, 2011; Volume 213, pp. 1–180.
60. Tõnsuaadu, K.; Gross, K.A.; Plüdüma, L.; Veiderma, M. A review on the thermal stability of calcium apatites. *J. Therm. Anal. Calorim.* **2012**, *110*, 647–659.
61. Langier-Kuźniarowa, A. *Thermograms of Clay Minerals*; Wydawnictwa Geologiczne: Warszawa, Poland, 1967; p. 315. (In Polish)
62. Morimoto, N.; Fabries, J.; Ferguson, A.K.; Ginzburg, I.V.; Ross, M.; Seifert, F.A.; Zussman, J.; Aoki, K.; Gottardi, G. Nomenclature of Pyroxenes. *Mineral. Mag.* **1988**, *52*, 535–550. [[CrossRef](#)]
63. Wen, X.; De Carlo, E.H.; Li, Y.H. Interelement relationships in ferromanganese crusts from the central Pacific ocean: Their implications for crust genesis. *Mar. Geol.* **1997**, *136*, 277–297. [[CrossRef](#)]
64. Manceau, A.; Marcus, M.A.; Grangeon, S. Determination of Mn valence states in mixed-valent manganates by XANES spectroscopy. *Am. Mineral.* **2012**, *97*, 816–827. [[CrossRef](#)]
65. Dubinin, A.V.; Sval'nov, V.N.; Uspenskaya, T.Y. Geochemistry of the Authigenic Ferromanganese Ore Formation in Sediments of the Northeast Pacific Basin. *Lithol. Miner. Resour.* **2008**, *43*, 91–110. [[CrossRef](#)]
66. Bolewski, A.; Osika, R.; Smakowski, T. *World Mineral Resources. Nickel-Ni, Cobalt-Co*; Wydawnictwa Geologiczne: Warszawa, Poland, 1984. (In Polish)

67. Varentsov, I.M.; Drits, V.A.; Gorschkov, A.I. Mineralogy, Geochemistry and Genesis of Manganese—Iron Crusts on the Bezymiannaya Seamount 640, Cape Verde Plate, Atlantic. In *Sediment-Hosted Mineral Deposits: Proceedings of a Symposium Held in Beijing, People's Republic of China, 30 July–4 August 1988*; Parnell, J., Lianjun, Y., Changming, C., Eds.; Blackwell Publishing Ltd.: Oxford, UK, 1990. [[CrossRef](#)]
68. Koschinsky, A.; Hein, J.R. Uptake of elements from seawater by ferromanganese crusts: Solid phase association and seawater speciation. *Mar. Geol.* **2003**, *98*, 331–351. [[CrossRef](#)]
69. Novikov, G.V.; Melnikov, M.E.; Bogdanova, O.Y.; Vikentev, I.V. Nature of Co-bearing ferromanganese crusts of the Magellan Seamounts (Pacific Ocean): Communication 1. Geology, mineralogy, and geochemistry. *Lithol. Miner. Resour.* **2014**, *49*, 3–25. [[CrossRef](#)]
70. Ostwald, J. Ferruginous vernadite in an Indian Ocean ferromanganese nodule. *Geol. Mag.* **1984**, *121*, 483–488. [[CrossRef](#)]
71. Wegorzewski, A.V.; Kuhn, T.; Dohrmann, R.; Wirth, R.; Grangeon, S. Mineralogical characterization of individual growth structures of Mn-nodules with different Ni + Cu content from the central Pacific Ocean. *Am. Mineral.* **2015**, *100*, 2497–2508. [[CrossRef](#)]
72. Burns, R.G.; Burns, V.M. Manganese oxides. In *Marine Minerals*; Burns, R.G., Ed.; Reviews of Mineralogy; Mineralogical Society of America: Washington, DC, USA, 1979; Volume 6, pp. 1–46.
73. Chukhrov, F.V.; Gorshkov, A.I.; Rudnitskaya, E.S.; Bierzovskaya, W.W.; Sivcov, A.W. Manganese minerals in clays: A review. *Clay Clay Miner.* **1980**, *28*, 346–354. [[CrossRef](#)]
74. Vodyanitskii, Y.V. Mineralogy and Geochemistry of Manganese: A Review of Publications. *Eurasian Soil Sci.* **2009**, *42*, 1170–1178. [[CrossRef](#)]
75. Grangeon, S.; Warmont, F.; Tournassat, C.; Lanson, B.; Lanson, M.; Elkaïm, E.; Claret, F. Nucleation and growth of feiknechtite from nanocrystalline vernadite precursor. *Eur. J. Mineral.* **2017**, *29*, 769–778. [[CrossRef](#)]
76. Manceau, A.; Lanson, M.; Takahashi, Y. Mineralogy and crystal chemistry of Mn, Fe, Co, Ni, and Cu in a deep-sea Pacific polymetallic nodule. *Am. Mineral.* **2014**, *99*, 2068–2083. [[CrossRef](#)]
77. Hochella, M.F.; Kasama, T.; Putnis, A.; Putnis, C.V.; Moore, J.N. Environmentally important, poorly crystalline Fe/Mn hydrous oxides: Ferrihydrite and a possibly new vernadite-like mineral from the Clark Fork River Superfund Complex. *Am. Mineral.* **2005**, *90*, 718–724. [[CrossRef](#)]
78. Novikov, G.V.; Melnikov, M.E.; Bogdanova, O.Y.; Drozdova, A.N.; Lobus, N.V. Mineralogy and Geochemistry of Co-bearing Manganese Crusts from the Govorov and Volcanologist Guyots of the Magellan Seamounts (Pacific Ocean). *Oceanology* **2017**, *57*, 716–722. [[CrossRef](#)]
79. Baturin, G.N.; Dubinchuk, V.T. Mineralogy and chemistry of ferromanganese crusts from the Atlantic Ocean. *Geochem. Int.* **2011**, *49*, 578–593. [[CrossRef](#)]
80. Muiños, S.B.; Hein, J.R.; Frank, M.; Monteiro, J.H.; Gaspar, L.; Conrad, T.; Pereira, H.G.; Abrantes, F. Deep-sea Fe-Mn Crusts from the Northeast Atlantic Ocean: Composition and Resource Considerations. *Mar. Georesources Geotechnol.* **2013**, *31*, 40–70. [[CrossRef](#)]
81. Chukhrov, F.V. Crystallochemical nature of Co-Ni asbolane. *Int. Geol. Rev.* **1982**, *24*, 598–604. [[CrossRef](#)]
82. Manceau, A.; Gorshkov, A.I.; Drits, V.A. Structural chemistry of Mn, Fe, Co, and Ni in manganese hydrous oxides: Part II. Information from EXAFS spectroscopy and electron and X-ray diffraction. *Am. Mineral.* **1992**, *77*, 1144–1157.
83. Dubinin, A.V.; Uspenskaya, T.Y.; Gavrilenko, G.M.; Rashidov, V.A. Geochemistry and Genesis of Fe–Mn Mineralization in Island Arcs in the West Pacific Ocean. *Geochem. Int.* **2008**, *46*, 1206–1227. [[CrossRef](#)]
84. Vodyanitskii, Y.V. Iron Hydroxides in Soils: A Review of Publications. *Eurasian Soil Sci.* **2010**, *43*, 1244–1254. [[CrossRef](#)]
85. Carlson, L.; Schwertmann, U. Natural occurrence of feroxyhite (δ -FeOOH). *Clays Clay Miner.* **1980**, *28*, 272–280. [[CrossRef](#)]
86. Burns, R.G.; Burns, V.M. Authigenic oxides. In *The Sea*; Emiliani, C., Ed.; J. Wiley & Sons, Inc.: Hoboken, NJ, USA, 1981; Volume 7, pp. 875–914.
87. Cornell, R.M.; Schwertmann, U. *The Iron Oxides: Structure, Properties, Reactions, Occurrences and Uses*, 2nd ed.; Wiley-VCH Verlag GmbH & Co. KGaA: Weinheim, Germany, 2003. [[CrossRef](#)]
88. Drits, V.A.; Sakharov, B.A.; Salyn, A.L.; Manceau, A. Structural model for ferrihydrite. *Clay Miner.* **1993**, *28*, 185–207. [[CrossRef](#)]

89. Taitel-Goldman, N.; Singer, A. High-resolution transmission electron microscopy study of newly formed sediments in the Atlantis II Deep Red Sea. *Clays Clay Miner.* **2001**, *49*, 174–182. [[CrossRef](#)]
90. Bogdanov, Y.A.; Vikent'ev, I.V.; Lein, A.Y.; Bogdanova, O.Y.; Sagalevich, A.M.; Sivtsov, A.V. Low-Temperature Hydrothermal Deposits in the Rift Zone of the Mid-Atlantic Ridge. *Geol. Ore Depos.* **2008**, *50*, 135–152. [[CrossRef](#)]
91. Buckley, H.A.; Bevan, J.C.; Brown, K.M.; Johnson, L.R.; Farmer, V.C. Glauconite and celadonite: Two separate mineral series. *Mineral. Mag.* **1978**, *42*, 373–382. [[CrossRef](#)]
92. Aspandiar, M.F.; Eggleton, R.A. Weathering of chlorite; II, Reactions and products in microsystems controlled by solution avenues. *Clays Clay Miner.* **2002**, *50*, 699–709. [[CrossRef](#)]
93. Palin, E.J.; Dove, M.T.; Hernández-Laguna, A.; Sainz-Díaz, C.I. A computational investigation of the Al/Fe/Mg order-disorder behavior in the dioctahedral sheet of phyllosilicates. *Am. Mineral.* **2004**, *89*, 164–175. [[CrossRef](#)]
94. Seyfried, W.E.; Shanks, W.C. Alteration of the upper oceanic crust at low temperatures. In *Hydrogeology of the Oceanic Lithosphere*; Davis, E., Elderfield, H., Eds.; Cambridge University Press: Cambridge, UK, 2004; pp. 451–494.
95. Obasi, C.C.; Terry, D.O., Jr.; Myer, G.H.; Grandstaff, D.E. Glauconite Composition and Morphology, Shocked Quartz, and the Origin of the Cretaceous(?) Main Fossiliferous Layer (MFL) in Southern New Jersey, U.S.A. *J. Sediment. Res.* **2011**, *81*, 479–494. [[CrossRef](#)]
96. Baldermann, A.; Dietzel, M.; Mavromatis, V.; Mittermayr, F.; Warr, L.N.; Wemmer, K. The role of Fe on the formation and diagenesis of interstratified glauconite-smectite and illite-smectite: A case study of Upper Cretaceous shallow-water carbonates. *Chem. Geol.* **2017**, *453*, 21–34. [[CrossRef](#)]
97. Margeta, K.; Logar, N.Z.; Šiljeg, M.; Farkas, A. Natural Zeolites in Water Treatment—How Effective is Their Use. In *Water Treatment*; Elshorbagy, W., Ed.; InTech: London, UK, 2013. [[CrossRef](#)]
98. Ijima, A.; Harada, K. Authigenic zeolites in zeolitic palagonite tuffs on Oahu, Hawaii. *Am. Mineral.* **1969**, *54*, 182–197.
99. Ciczyszili, G.W.; Andronikaszwili, T.G.; Kirkow, G.N.; Filizowa, L.D. *Natural Zeolites*; WNT: Warszawa, Poland, 1990. (In Polish)
100. Dubinin, A.V. Geochemistry of rare earth elements in oceanic phillipsites. *Lithol. Miner. Resour.* **2000**, *35*, 101–108. [[CrossRef](#)]
101. Stonecipher, S. *Natural Zeolites: Occurrence, Properties, Use*; Pergamon Press: Oxford, UK, 1978; pp. 221–234.
102. Neuhoff, P.S.; Rogers, K.L.; Stannius, L.S.; Bird, D.K.; Pederson, A.K. Regional very low-grade metamorphism of basaltic lavas, Disko-Nuussuaq region, West Greenland. *Lithos* **2006**, *92*, 33–54. [[CrossRef](#)]
103. Voudouris, P.; Psimis, I.; Mavrogonatos, C.; Kanellopoulos, C.; Kati, M.; Chlekou, E. Amethyst occurrences in Tertiary volcanic rocks of Greece: Mineralogical and genetic implications. *Bull. Geol. Soc. Greece* **2013**, *47*, 477–486. [[CrossRef](#)]
104. Pe-Piper, G.; Miller, L. Zeolite minerals from the North Shore of the Minas Basin, Nova Scotia. *Atl. Geol.* **2002**, *38*, 11–28. [[CrossRef](#)]
105. Hughes, J.M.; Rakovan, J.F. Structurally robust, chemically diverse: Apatite and apatite supergroup minerals. *Elements* **2015**, *11*, 165–170. [[CrossRef](#)]
106. Bouzari, F.; Hart, C.J.R.; Bissig, T.; Barker, S. Hydrothermal Alteration Revealed by Apatite Luminescence and Chemistry: A Potential Indicator Mineral for Exploring Covered Porphyry Copper Deposits. *Econ. Geol.* **2016**, *111*, 1397–1410. [[CrossRef](#)]
107. Marino, E.; González, F.J.; Somoza, L.; Lunar, R.; Ortega, L.; Vázquez, J.T.; Reyes, J.; Bellido, E. Strategic and rare elements in Cretaceous-Cenozoic cobalt-rich ferromanganese crusts from seamounts in the Canary Island Seamount Province (northeastern tropical Atlantic). *Ore Geol. Rev.* **2017**, *87*, 41–61. [[CrossRef](#)]
108. Hein, J.R.; Koschinsky, A.; Mikesell, M.; Mizell, K.; Glenn, C.R.; Wood, R. Marine Phosphorites as Potential Resources for Heavy Rare Earth Elements and Yttrium. *Minerals* **2016**, *6*, 88. [[CrossRef](#)]
109. Sha, L.K.; Chappell, B.W. Apatite chemical composition determined by electron microprobe and laser-ablation inductively coupled plasma mass spectrometry, as a probe into granite petrogenesis. *Geochim. Cosmochim. Acta* **1999**, *63*, 3861–3881. [[CrossRef](#)]

110. Guptha, M.V.; Banerjee, R.; Mergulhao, L. On the nature of the calcareous substrate of ferromanganese crust from the Vityaz Fracture Zone, Central Indian Ridge: Inferences on paleoceanography. *Geo-Mar. Lett.* **2002**, *22*, 12–18. [[CrossRef](#)]
111. Nishi, K.; Usui, A.; Nakasato, Y.; Yasuda, H. Formation age of the dual structure and environmental change recorded in hydrogenetic ferromanganese crusts from Northwest and Central Pacific seamounts. *Ore Geol. Rev.* **2017**, *87*, 62–70. [[CrossRef](#)]



© 2019 by the authors. Licensee MDPI, Basel, Switzerland. This article is an open access article distributed under the terms and conditions of the Creative Commons Attribution (CC BY) license (<http://creativecommons.org/licenses/by/4.0/>).